A novel laser-based method to measure the adsorption energy on carbonaceous surfaces

D. Duca, C. Pirim, M. Vojkovic, Y. Carpentier, A. Faccinetto, M. Ziskind, C. Preda, C. Focsa

A novel laser-based method to measure the adsorption energy on carbonaceous surfaces

D. Duca[a], C. Pirim[a], M. Vojkovic[a], Y. Carpentier[a], A. Faccinetto[b], M. Ziskind[a], C. Preda[c], C. Focsa[a,*]

[a] *Univ. Lille, CNRS, UMR 8523 – PhLAM – Laboratoire de Physique des Lasers Atomes et Molécules, F-59000 Lille, France*
[b] *Univ. Lille, CNRS, UMR 8522 – PC2A – Physicochimie des Processus de Combustion et de l'Atmosphère, F-59000 Lille, France*
[c] *Univ. Lille, CNRS, UMR 8524 – Laboratoire de Mathématiques Paul Painlevé, F-59000 Lille, France*

Abstract

The reactivity of carbonaceous surfaces bears a fundamental role in various fields, from atmospheric chemistry and catalysis to graphene and nanoparticles. This reactivity is mainly driven by the surface chemical composition and by the strength of the interaction between the adsorbates and the surface (physi-/chemisorption). While the surface composition of complex natural samples can be well characterized, adsorption energies (ergo, adsorption processes) of the corresponding adsorbate/adsorbent systems are often overlooked. We propose a novel laser-based method for measuring the adsorption energy of chemical species on various carbonaceous surfaces. The proof of concept of this original method has first been demonstrated by deriving adsorption energies of various systems consisting of polycyclic aromatic hydrocarbons and activated carbon. The great potential of this fast, spatially resolved, and surface-sensitive method, which can also act as a defect density probe at the mesoscale, has been further demonstrated through the study of systems of increasing complexity.

Keywords: Carbonaceous surfaces, Adsorption energy, Laser-induced thermal desorption, Mass spectrometry, Bayesian statistics

1. Introduction

Carbonaceous materials are used in a wide range of applications including aerospace and defense, automotive, energy, construction, electronics, and sports. Their superior properties including excellent stiffness, high tensile strength, low thermal expansion, and good temperature tolerance [1, 2], make them versatile materials that can be shaped into various forms depending upon the use intended (*e.g.* carbon fibers, carbon nanotubes, graphene). Carbon-based materials can also be turned into metal-free catalysts and serve as a promising alternative to transform sustainable biomass into renewable energy systems [3].

Due to their excellent adsorption capacities, carbonaceous materials are widely employed as filtration media. Carbon nanotubes (CNT) show great potential at revolutionizing water and gas treatment technologies [4] as they provide much higher surface areas, adsorption capacities, and faster kinetics than activated carbon, the currently prevailing filtration agent. The utility of the adsorptive fixation of organics in the gas and liquid phases for treating wastewaters and emission gasses is already showcased for a number of harmful compounds [5–8]. Another considerable advantage of carbon nanostructures is that their properties can be tailored to target certain chemical species (e.g toxins, heavy metal ions) [4, 9, 10].

For carbonaceous materials, the downside of exhibiting high adsorptive capacities is that they will act as surface carriers. This can lead to adsorbed toxic species undergoing long-range transport in the atmosphere. This effect is commonly observed with combustion generated aerosols (soot), which consist of a carbonaceous matrix often coated with a plethora of organic species [11–13], many of them exhibiting a proven carcinogenic potential [14–16].

*Corresponding author. Tel.: +33 675 482 049
Email address: cristian.focsa@univ-lille.fr (C. Focsa)

This makes the impact of combustion generated particles on human health considerably greater, especially since their inhalation can result in health problems beyond the lungs [17]. In fact, the presence of combustion derived nanoparticles has been detected in the frontal cortex of autopsy brain samples [18], urine of healthy children [19], and even in the fetal side of the placenta [20]. If transported to the fetus, these particles – as surface carriers for potentially toxic species – could significantly affect fetal health and development [20].

In this context, the benefit of identifying the adsorption mechanism on carbonaceous surfaces and its associated adsorption energy is threefold. It can provide necessary information to better comprehend, and potentially minimize, the health impact of carbonaceous aerosols. It can help design better carbon-based materials for industrial use. And finally, it can offer some insights into the complex and still only partially understood soot formation mechanism since adsorption energies define whether the surface species (adsorbates) are chemisorbed or physisorbed, and therefore if the surface molecular compounds result from surface chemistry (remnants of the soot formation) or physical condensation [21].

Adsorption performances are governed by physical and chemical parameters that greatly vary across adsorbate/adsorbent systems. Thus, a systematic study needs to be undertaken in order to determine i) to what extent the adsorption energy depends on the nature and the size of the adsorbate, and ii) the type of interactions established between adsorbate and adsorbent. Depending upon the nature of the adsorbate (gas or liquid) and adsorbent (polycrystalline film, single-crystal, oxides, or nanoparticle surfaces, powders suspended in a liquid or loose powders) [22], various microcalorimetry techniques, such as single-crystal adsorption calorimetry (SCAC), isothermal titration calorimetry (ITC), and differential scanning calorimetry (DSC) [23, 24], or temperature-programmed desorption (TPD) [25, 26] are commonly used to either measure directly the heat of adsorption (microcalorimetry) [27–29], or infer the activation energy for desorption (TPD). However, for systems exhibiting meso or macro scale (micrometer- or submillimeter sized) inhomogeneities or field-collected samples exhibiting small quantities of matter and complex compositions (*i.e.* with a multitude of co-adsorbed species), the use of these conventional techniques becomes at best arduous and at worst impossible.

We propose here an original solution to overcome the restrictions encountered with more conventional techniques when determining adsorption energies. Our method relies on laser-induced thermal desorption (LITD) coupled with ultra-sensitive mass spectrometry detection. The principle of the method relies on the following stages: the carbonaceous sample surface is very rapidly heated by a (visible) nanosecond laser pulse. The heating is local (scale of the laser beam diameter) and transient (initial temperature regained on a microsecond time scale). A fraction of the molecules adsorbed on the sample surface is therefore desorbed and subsequently ionized by a second (UV) laser pulse before being mass-selectively detected by a time-of-flight mass spectrometer. Low desorption and ionization laser fluences are used to prevent fragmentation of the analytes or alteration of the adsorbent. The fraction of molecules desorbed from an irradiated spot depends on the laser fluence and the number of pulses it is exposed to. These relationships are specific to each adsorbate/adsorbent system and indicative of the interaction between the two components. The resulting experimental data can then be mathematically treated to derive the corresponding adsorption energy.

We present in this paper two distinct experimental approaches, derived from the same LITD principle, along with two mathematical models (and associated statistical procedures) we developed to retrieve the adsorption energy from the recorded experimental data. The method is validated on well-controlled laboratory-synthesized samples, associating several carbonaceous adsorbents and organic/inorganic adsorbates at sub-monolayer concentration, in a broad range of adsorption energies (0.2 – 1.5 eV).

2. Materials and Methods

2.1. Experimental approaches

Two distinct approaches based on the LITD principle were followed to collect experimental data for adsorption energy determination: the "signal decay" and the "fluence curve".

2.1.1. Signal decay

The principle of this first experimental approach is presented in Fig. 1a-c: a region of the sample

(delimited by the laser spot on the surface) is irradiated with successive nanosecond laser pulses (10 Hz repetition rate) of constant (low) fluence. For each pulse, a fraction of desorbed molecules is ionized by a second nanosecond laser and further detected by a mass spectrometer. Mass spectra are so recorded for successive laser pulses and the signal corresponding to the adsorbate of interest is plotted as a function of the number of applied laser pulses (Fig. 1c). The pseudo-exponential decay observed simply illustrates a gradual "cleaning" of the irradiated spot by the successive desorption pulses. If this decay is "slow" (*i.e.* a high number of laser pulses is needed to "clean" the surface), then one can infer a strong interaction between the adsorbate and the surface. Conversely, a faster decay (in the same irradiation conditions) will be indicative of looser bonding of the adsorbate to the surface.

2.1.2. Fluence curve

The second approach relies on the variation of the desorption yield with the laser fluence, as illustrated in Fig. 1d-e. In this approach, multiple spots on the sample surface are irradiated with only one pulse each, but the pulses exhibit different fluences. Each measurement is performed on different spots of the sample, *i.e.* on a pristine surface that was not previously irradiated, to ensure that the initial concentration is always the same. The different fluences will lead to different temperature increase for each spot and, consequently to different desorption yields. Fitting the fluence variation of the desorption yield with the adequate equation (see below) allows retrieving the adsorption energy.

2.2. L2MS set-up

The experimental setup used in this work is based on the L2MS technique [11, 30, 31], which combines three key stages: laser desorption (LD), laser ionization (LI), and time-of-flight mass spectrometry (ToF-MS). The sample is mounted onto a copper holder maintained at constant temperature (170 – 190K in this study) by a regulating device consisting of a heating resistor and a liquid nitrogen closed loop. Initially developed for studies on ice samples [32, 33], this system has proved its efficiency in preventing volatile analyte evaporation at the working pressure ($\sim 10^{-8}$ mbar) of the mass spectrometer on many combustion-related [11, 30, 34, 35] or PAH-containing [31, 36] samples.

The sample surface (placed vertically, Fig. 2) is irradiated at normal incidence by the 4 ns pulsed beam of an Nd:YAG laser (Continuum Minilite, second harmonic, $\lambda = 532$ nm). The desorption laser beam hits the surface with a quasi-top-hat profile of $\sim$0.7 mm diameter (measured with a Gentec Beamage-4M beam profiler). The quasi top-hat transverse intensity profile is obtained from the laser output beam by first enlarging it with a beam expander built around a set of convergent and divergent lenses, and then selecting the quasi-flat central region ($\sim$5%) of the beam with a diaphragm, which is further image relayed onto the sample surface using a convergent lens.

The desorbed neutral molecules form a forward-peaked plume (*i.e.* narrow angular distribution around the revolution symmetry axis) which propagates at high speed [31, 37] from the sample surface toward the ionization zone. Neutral molecules from the desorbed plume are ionized following a two-photon ionization process [30, 38] using another 4 ns pulsed laser beam (Continuum Powerlite, $\lambda = 266$ nm, 10 Hz repetition rate, $\sim$1 mm diameter, top-hat) propagating orthogonally (y direction, Fig. 2) to the desorption plume axis. The ionization laser beam intercepts the desorption plume in between the extraction electrodes of an 1 m long, reflectron time-of-flight mass spectrometer (RM Jordan, mass resolution $m/\Delta m \sim 1000$) at $d \sim 3$ cm from the sample surface. The delay between the desorption and ionization pulses is set to 100 μs by a digital delay/pulse generator (SRS DG535).

The ions thus generated are extracted and accelerated (x direction) toward the free-field flight tube of the mass spectrometer. Mass spectra are recorded with a digital oscilloscope (LeCroy Waverunner 6200A) at a time resolution of 2 ns/point. Data acquisition is controlled by a dedicated routine developed in LabView (National Instruments). Experimental data points considered in this work and amenable to mathematical treatment represent integrated peak areas corresponding to a given analyte, which includes all the peaks associated with its isotopic distribution.

2.3. Surface evolution upon irradiation

The desorption fluence is carefully adjusted to be in the low, pre-ablation regime [11, 30], which ensures the desorption of neutral species from the surface of the sample without affecting the underlying carbonaceous matrix. Upon irradiation, the sample surface undergoes temperature variations of large magnitude (1500–2000 K) over a

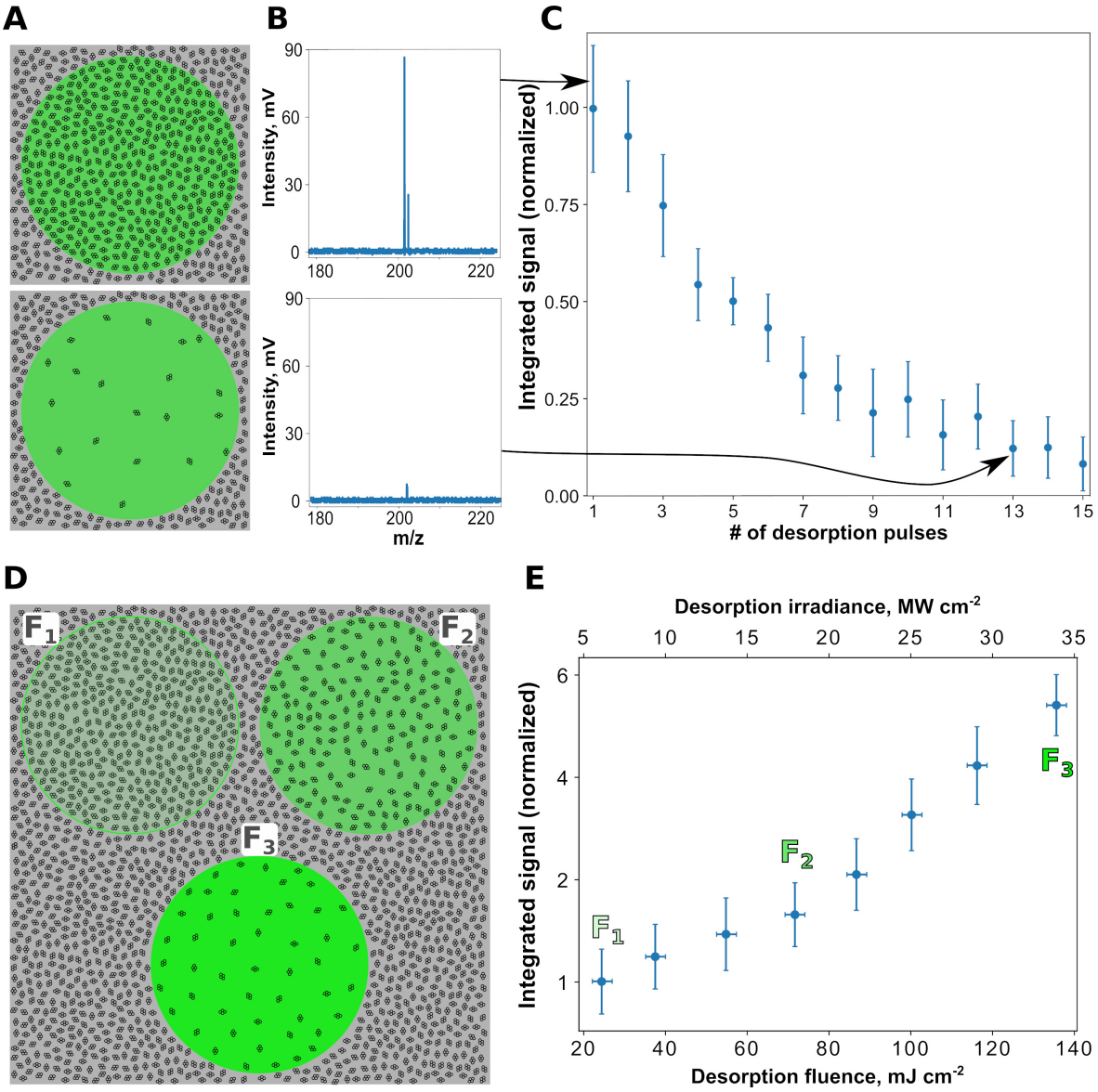

Figure 1: The top and bottom rows describe the "signal decay" and the "fluence curve" experimental approaches, respectively, used to obtain the two distinct datasets from which adsorption energies were subsequently derived. (a) Schematics of the adsorbate coverage evolution upon successive laser pulses of constant fluence applied on the same spot on the sample surface, (b) recorded mass spectra corresponding to two distinct desorption laser pulses (top – 1^{st} pulse, bottom – 13^{th} pulse), and (c) recorded signal decay. (d) Schematics of the "fluence curve" approach – different spots of the sample irradiated with single laser pulses of various fluences, (e) recorded "fluence curve" signal.

very short period of time (the surface typically regains its initial temperature in about 1 μs). Despite the high temperature reached by the surface (for only nanoseconds), it was demonstrated that such a fast-transient process, when generated with low fluence pulses as performed here, does not ablate the adsorbent [11]. Moreover, our fluence optimization procedure shows that mass spectra are devoid of any fragments originating from the adsorbate throughout the whole fluence regime used in this work. Therefore, our measurements demonstrate that such fluence regime prevents the fragmentation of the desorbed molecules and precludes ablation of the adsorbent.

In regards to possible adsorbent nanostructure rearrangement upon fast-transient heating, previ-

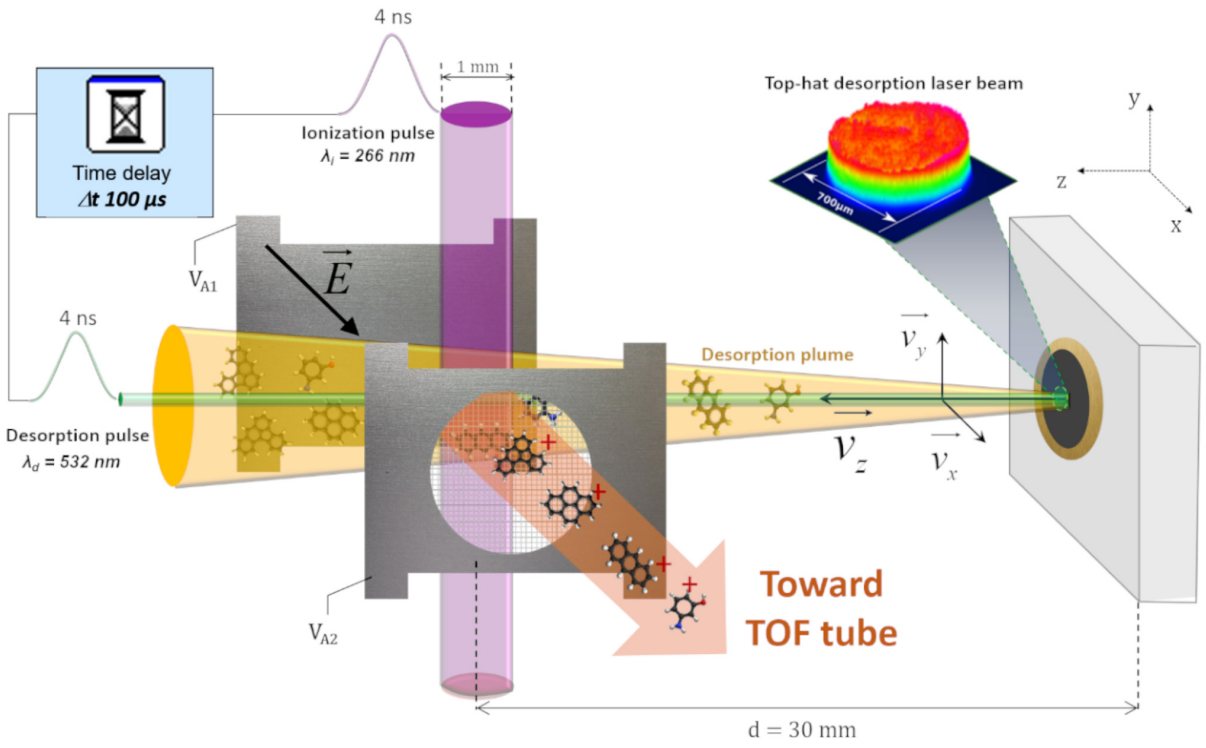

Figure 2: Schematic representation of the laser desorption / laser ionization / ToF-MS experimental arrangement. The desorption laser beam (green) with a top-hat transverse beam profile forms a 700 μm spot on the sample surface. The desorbed neutral molecules form a "plume" (dark yellow) which propagates from the sample surface (z axis) toward the ionization region situated in between the extraction electrodes of the ToF-MS. A pulsed UV ionization laser beam (purple, y axis) intersects the desorption plume 100 μs after the desorption beam hits the surface. The obtained ions are then extracted and accelerated (x axis) toward the field-free flight tube of the ToF-MS.

ous works on amorphous carbon films [39] or black carbon nanoparticles [40] irradiated by nanosecond Nd:YAG laser pulses showed that no significant change in the sample structure was induced in the low fluence regime (typically < 50 mJ cm^{-2}). In the work of Abrahamson et al. [40], multi-wavelength pyrometry was used to measure transient surface temperatures of more than 2000°C, while no notable difference in carbon nanostructure was observed by transmission electron microscopy (*i.e.* no rearrangement).

In the first ("signal decay") experimental approach followed in our work, when a single region of the surface (adsorbent) is irradiated with successive nanosecond laser pulses resulting in the gradual desorption of the adsorbate, it is worth noting that the changing adsorbate surface concentration upon subsequent irradiations does not affect the thermal and optical properties of the system as long as the chemical species are transparent to the desorption pulse ($\lambda_d = 532$ nm) and as the system exhibits a very low surface coverage (both conditions met in this work). As the L2MS technique involves the fast removal of species from the vicinity of the sample [31, 37], re-adsorption of desorbed species is negligible. In addition, any lateral diffusion of molecules across the surface that could potentially replenish the laser spot in between two consecutive desorption laser pulses (100 ms) can be neglected. For instance, it would take minutes for a pyrene molecule to travel a distance of 1 μm on a carbon surface [41]. Therefore, the physical characteristics of the sample will not change with the increasing number of desorption pulses and thus not influence the desorption process.

2.4. Sample preparation

The development and validation of a method for adsorption energy determination requires well characterized samples. Moreover, the reproducibility of

the method could be assessed only if the characteristics of the sample are held constant. As this work focuses on desorption from carbonaceous surfaces, combustion-generated particles (soot) would have been an appealing candidate as object of study, however, they usually exhibit a very high variability, as their characteristics (*e.g.* specific surface, porosity) depend highly on the combustion conditions. In this context, laboratory-prepared "synthetic soot" [11] represents an interesting alternative as it exhibits a structure akin to that of real soot but has a known and controllable surface chemical composition.

Synthetic soot is prepared here following the protocol described in our previous work [11]. Briefly, polycyclic aromatic hydrocarbons (pyrene and coronene, Sigma Aldrich, 98% purity) are dissolved into dichloromethane (Sigma Aldrich, 99% purity) to make mother (stock) solutions of known concentrations. To these stock solutions are added activated carbon particles (Pureblack 100 Carbon, average particle diameter 80 nm, specific surface area 80–150 m^2g^{-1}) and the resulting mixtures are magnetically stirred for 2 hours. The mixtures are then filtered using a vacuum filtration system employing a quartz fiber filter (Pall Tissuquartz QAT- UP 2500). This filtration step yields, on the one hand, a quartz fiber filter covered by a submillimeter thick soot layer infused with the stock solution, and, on the other hand, a filtered solution whose remaining concentration in PAHs can be determined by UV-Vis absorption spectroscopy and subsequent comparison with the stock solution (see Figure S1a). Specifically, as the measured absorbance and the molar concentration are directly proportional in the concentration range studied here, molar concentrations can be estimated knowing the molar extinction coefficient of the solution at a given wavelength and path length. From absorbance measurements of stock solutions of known concentrations can thus be deduced the molar concentrations of the filtered solutions. Therefore, by comparing the absorbance of the stock solution and that of the filtered solution (Figure S1b), it is possible by difference to retrieve the concentration of PAHs remaining on the filter, assuming volatility losses during the preparation steps are negligible [11]. Finally, the surface concentration of PAHs adsorbed on activated carbon particles is calculated knowing the PAH concentration and the specific surface of the particles deposited on the filter.

Three different samples containing either organic or inorganic species were prepared using the described procedure (Table 1). This included systems containing either a single or two co-adsorbed compounds. Pyrene and coronene were chosen here as adsorbates because of the well-known presence of polycyclic aromatic hydrocarbons (PAH) on the surface of soot particles sampled from real combustors [11, 12]. Additionally, Pb – a heavy metal commonly found in industrial wastewater and usually removed using various carbonaceous materials [9, 10], was used to validate the method for inorganic species. A similar protocol (but a different solvent – ultra-pure deionized water, Purelab Option-Q) was used for the preparation of the lead samples from $PbCl_2$ salt (Sigma Aldrich, 98%) and Pureblack activated carbon.

Table 1: List of the samples synthesized for adsorption energy measurements. The surface coverage θ (in monolayers, ML) was determined from UV-Vis extinction measurements.

Sample	**θ, ML**
Pyrene / activated carbon	$2{\cdot}10^{-3}$
(Pyrene + coronene) / activated carbon	$8{\cdot}10^{-3}$ (pyrene) $1.2{\cdot}10^{-2}$ (coronene)
Pyrene / graphite sheet	$\lesssim 10^{-3}$
Pyrene / HOPG	$\lesssim 10^{-3}$
Pb / activated carbon	$\lesssim 10^{-3}$

In order to study the influence of the surface defect density on the retrieved adsorption energy, two more samples based on (mm-thick) graphite sheet and highly oriented pyrolitic graphite (HOPG) adsorbents were prepared in a similar way as the synthetic soot, with the exclusion of the vacuum filtration step. Graphite (Alfa Aesar, graphite sheet) and HOPG (Sigma Aldrich) exhibit significantly lower specific surface areas compared to activated carbon. The resulting adsorbate surface concentration is therefore at the limit of detection of the spectrophotometric method [11]. For this reason, only upper coverage limits ($\sim 10^{-3}$ ML) are provided in Table 1.

Considering the low coverages and the preparation protocol used in this work, we can assume first that no lateral interaction between adsorbate molecules is present, and second that the coverage is homogeneous across the surface. A low coverage also reduces the possibility of adsorbates forming islands of stacked molecules [42] and thus ensures that the only interaction probed is between adsorbates and the adsorbent surface. Moreover, under these experimental conditions any lateral diffusion

of molecules across the surface that could potentially replenish the irradiated spot between desorption laser pulses can be neglected [41].

2.5. Repeatability

To account for possible experimental fluctuations (mainly due to desorption and ionization lasers), several equivalent measurements are performed in different zones of the same sample. The analyzed regions are chosen not to overlap and therefore all measurements are considered self-contained. Specifically, for the first experimental approach (signal decay), four signal decays are recorded for the same laser set-point, each decay in a pristine sample zone. For the second experimental approach (*i.e.* fluence curve), four experimental data points per desorption fluence value are acquired on four distinct (pristine) zones of the sample (*e.g.* for pyrene, seven desorption fluence values are utilized which results in 28 experimental datapoints in total). As all measurements are performed in different spots on the sample, each datapoint is fully independent. Therefore, different combinations of these points can be made to build distinct "fluence curves". Among all possible combinations, a total of 10 distinct fluence curves are constructed by randomly combining experimental datapoints.

3. Theory

3.1. Background

When a pulsed laser beam hits a sample surface, a part of its energy (determined by the physical properties of the irradiated material) is passed on to the sample and induces a temperature jump that may i) trigger the desorption of adsorbates possibly present on the surface, ii) alter the surface (nanostructure changes), or even iii) ablate micro-volumes of sample. This study is performed in the framework of the first effect, known as laser-induced thermal desorption (LITD). The pulsed laser-induced heating increases the temperature of surfaces at high rates (up to $\sim 10^{11}$ $\mathrm{K\,s^{-1}}$ with a nanosecond laser [43]), otherwise unattainable with traditional methods (*e.g.* resistive or electron bombardment heating), and is therefore appealing for application to desorption studies. Early studies showed efficient desorption of H, CO, and CO_2 molecules from a variety of surfaces irradiated by pulsed laser beams [44], phenomenon interpreted as a purely thermal effect. This effect was later used to study the adsorption and desorption kinetics of these species by means of relaxation methods [45]. LITD was also used to examine the desorption of Na and Cs atoms with a sub-monolayer surface concentration from Ge (100) substrates [46], of H_2 from Ni (100), (110) and (111) [45], of CO from Fe [47] and of benzene from Pt (111) surfaces [48]. However, none of these studies addressed the determination of the adsorption energies from LITD data, as they typically used a single high-fluence laser pulse to desorb all the adsorbed species from the surface, thereby completely "cleaning" the irradiated spot of the sample with only one laser pulse. On the other hand, when a lower desorption laser fluence is used, not all the molecules are desorbed by a single laser pulse and multiple, consecutive pulses can be applied to the same surface spot [49]. Since after each desorption pulse the surface concentration of molecules reduces, the amount of desorbed compounds decreases after each subsequent laser pulse, thus resulting in a pseudo-exponential variation of both surface coverage and desorbed amount. This variation was first linked to the energetics of the adsorbate-adsorbent interaction by Specht and Blades [21], who suggested that the decay obtained for pyrene desorbing from charcoal corresponds to molecules that are weakly bound to the surface, while the relatively constant signal that followed was associated with molecules having a stronger interaction with the carbonaceous surface. The observed decay, however, was not used by the authors to derive the strength of the pyrene-surface interaction.

A similar decay was reported by our laboratory in a previous work [11] which focused on the calculation of the detection limit of the two-step laser mass spectrometry (L2MS) technique. Although the energetics of the analyte-surface bond was not studied, we demonstrated at that time that a single form of interaction between the analyte and the carbonaceous surface (in this case physisorption) can be achieved on surrogate soot samples. A different approach was proposed by Dreisewerd et al. [50] to derive the activation energy of desorption from sinapic acid and bovine insulin thick layers deposited on stainless steel, based on the evolution of the desorbed amount of molecules with the irradiation laser fluence.

The present study builds on this previous works and proposes for the first time a complete experimental, theoretical, and data treatment methodol-

ogy to derive adsorption energies from LITD/L2MS experiments. Moreover, by developing a theoretical model describing LITD, an extra step was taken toward better understanding fast processes occurring at the sample surface.

3.2. Desorption of physisorbed species

In the kinetic approach, the desorption is described in terms of the desorption rate – the number of molecules that desorb from a unit of surface per unit of time. Assuming that all adsorbed atoms or molecules occupy identical sites, the desorption rate can be expressed by the Polanyi-Wigner equation [51]:

$$-\frac{d\theta}{dt} = \nu\theta^n \exp\left(-\frac{E_{des}}{k_B T}\right) \quad (1)$$

where n is the order of the desorption kinetics (usually $n = 1$ for physisorption), E_{des} is the activation energy for desorption, T is the surface temperature, and k_B the Boltzmann constant. As said above, at the low adsorbate coverages used here (10^{-3}–10^{-2} monolayers) any interaction between neighbouring adsorbed molecules can be neglected [52], and thus the E_{des} will be characteristic of the adsorbate-adsorbent interaction only. The first-order pre-exponential factor ν (measured in s^{-1}), related with the vibration of the adsorbate-adsorbent bond along the reaction coordinate associated with desorption, is also called attempt frequency and is on the order of the atomic frequency of the crystal lattice ($\sim 10^{13}\,\mathrm{s}^{-1}$) [53]. For the atom or molecule to leave the surface it needs to overcome the activation barrier for desorption. Since physisorption is a reversible process, the activation energy of desorption is equal to the adsorption energy: $\mathrm{E}_{ads} = \mathrm{E}_{des}$, and therefore these two terms will be used interchangeably hereafter.

As seen in Eq. (1), the driving force of desorption is the surface temperature. Therefore, to calculate the rate of desorption and subsequently estimate the adsorption energy, one should first determine the temperature variation. A precise calculation of the temperature temporal and spatial variation involves quite a heavy mathematical apparatus. Therefore, some authors [50, 54, 55] have used a simplified LITD description, a steady-state process involving an "effective" temperature that would be reached upon laser irradiation and at which the desorption occurs.

Although a more elaborated, space- and time-resolved model was developed in this study, we also present here this simplified approach for the sake of comparison with previous works.

3.3. "Effective temperature" model

The advantage of this simplified, steady-state approach is that all optical and thermal properties of the sample are expressed by a single factor, thus making it easier to retrieve when fitting experimental data. Moreover, the temperature profile of the sample is not required which significantly reduces the computational time needed by the model. Within this approximation, the number of molecules N desorbed after a laser pulse can be expressed as [50, 54, 55]:

$$N \approx A \cdot \exp\left(\frac{-E_{ads}}{k_B\,(T_0 + BF)}\right) \quad (2)$$

where A is proportional to the surface coverage, B is a factor that describes the conversion of the deposited energy into the surface temperature increase and is associated (for the low coverage used here) solely with the adsorbant properties, T_0 is the initial temperature, F the desorption laser fluence at the surface. In this model, $(T_0 + BF)$ is seen as an "effective" sample temperature which would be reached upon laser irradiation and at which the desorption occurs.

The energy deposited into the sample unit volume is determined by the incident laser fluence, and accounts for the reflectivity R and the optical absorption coefficient $\alpha(\lambda_0)$ of the sample at the desorption laser wavelength λ_0. This is expressed through the B parameter, as follows [50]:

$$B = (1 - R)\frac{\alpha(\lambda_0)}{\rho c} \quad (3)$$

where c is the specific heat capacity of the sample and ρ is the sample density. The value of the B parameter can considerably change depending on the actual sample characteristics; however, a good initial estimation can be obtained with values reported in the literature. Alternatively, B can be determined by measuring the required physical parameters of the sample prior to the adsorption energy determination. However, this is not always possible in the case of field-collected samples since characterizing micrograms of material can be challenging and adds extra preparation steps that can potentially damage and/or contaminate the sample (often being very expensive to obtain and/or unique). Therefore, the developed model should be

able to determine the adsorption energy based on only an 'initial guess' for the B parameter. The B parameter values calculated for two different adsorbent materials used in this work (nano-porous soot and graphite), along with the physical constants used in their calculation, are presented in Table 2. Note that the B values presented in this table can be only seen as estimates, sufficiently close to the real values to be used by the fitting algorithm as 'initial guess'.

Table 2: B parameters calculated from Eq. (3) for activated carbon particles and graphite, along with physical parameters sourced from the literature and used in the calculation.

Parameter	**Carbonaceous surface**	
	Activated carbon particles	**Graphite**
R	0.2^a	0.1^b
α, $10^7 m^{-1}$	$1.0951^{c,d}$	3.4385^b
ρ, $10^3 kg\,m^{-3}$	0.4^c	1.9^d
c, $J\,K^{-1}\,kg^{-1}$	840^c	$970^{d,e}$
B, $J^{-1}\,K\,m^2$	26.0	16.2

^{a}Ref. [56], ^{b}Ref. [57], ^{c}Ref. [11], ^{d}Ref. [58], ^{e}Ref. [59]

The surface concentration of adsorbed species decreases after each desorption pulse, changing the A factor in Eq. (2). The first laser pulse will give N_1 desorbed molecules:

$$N_1 = p \cdot s \cdot Q_0 \cdot \exp\left(-\frac{E_{ads}}{k_B(T_0 + BF)}\right) \quad (4)$$

where Q_0 is the initial adsorbate surface concentration, s is the surface area of the irradiated spot, and p a proportionality constant. The number of molecules left on the irradiated surface spot will progressively decrease after each subsequent laser pulse.

Considering that for the low coverages used here the adsorption energy does not change with the surface concentration (see Section 2.4) and the physical properties of the sample surface do not change upon irradiation with successive laser pulses (see Section 2.3), N_j molecules will be desorbed on the j^{th} desorption pulse:

$$N_j = p{\cdot}s{\cdot}Q_0\left(1 - p \cdot \exp\left(-\frac{E_{ads}}{k_B(T_0 + BF)}\right)\right)^{j-1} \cdot \exp\left(-\frac{E_{ads}}{k_B(T_0 + BF)}\right) \quad (5)$$

The S_j signal recorded by the detector will therefore be:

$$S_j = m \cdot N_j = m \cdot p \cdot s \cdot Q_0\left(1 - p \cdot \exp\left(-\frac{E_{ads}}{k_B(T_0 + BF)}\right)\right)^{j-1} \cdot \exp\left(-\frac{E_{ads}}{k_B(T_0 + BF)}\right) \quad (6)$$

where m is a proportionality factor accounting for the ionization efficiency, transfer function of the mass spectrometer, and detector efficiency.

The variation of the recorded signal can also be expressed as a function of the desorption fluence – a "fluence curve" that can be obtained with the second experimental approach (see Section 2.1.2):

$$S(F) = m \cdot p \cdot s \cdot Q_0 \cdot exp\left(-\frac{E_{ads}}{k_B(T_0 + BF)}\right) \quad (7)$$

The proposed model can be used to derive the adsorption energy of a given analyte from experimental data recorded by the mass spectrometer. The adsorption energy of an analyte can be retrieved by fitting experimental data either with Eq. (6) (signal decay induced by successive laser pulses applied on the same surface spot) or Eq. (7) (signal variation with fluence). The fitting algorithm requires an "initial guess" – a starting point relatively close to the actual values. The initial guess for the B parameter was calculated using literature data (Table 2). The initial value for the adsorption energy was also sourced from the literature (*e.g.* 0.98 eV for pyrene [60, 61]). We note however that fitting the signal decay and fluence curves with Eq. (6) and (7), respectively, can be challenging as they contain two highly correlated parameters. Since the "effective" temperature reached by the surface upon laser irradiation is significantly higher than its initial temperature (*i.e.* $BF \gg \mathrm{T}_0$), the adsorption energy E_{ads} and the B parameter are highly correlated. Therefore, fitting the proposed model to experimental data requires a specific algorithm which is detailed below in Section 3.5 and Appendices A and B.

3.4. Transient temperature model

3.4.1. Pulsed laser surface heating

The effective temperature desorption model is only a crude approximation of the laser-induced thermal desorption and to fully model this process the fast variation of the sample temperature

should be taken into account. A variety of studies addressed the fast heating of solid samples exposed to lasers, describing the processes occurring at different wavelengths, laser irradiances, pulse lengths and on various target materials [11, 49, 62–66]. The approach commonly followed is to describe laser–solid interactions at a macroscopic scale using the heat conduction equation (although some studies treated this phenomenon at an atomistic/molecular level, but on a limited timescale [54]). For low-fluence nanosecond laser pulses, the energy passed on to the sample does not lead to its melting nor its evaporation, therefore no phase transition terms are needed in the equations [64]. Most of the studies focus on the temperature variation in the sample volume (*i.e.* along the z depth axis) and not radially on the surface. Moreover, the laser pulse is often considered as a surface heat source (z=0), which does not take into account its propagation into the sample volume as described by the Beer-Lambert law [11].

To calculate sample temperature variations upon laser irradiation, the sample was considered as a medium characterized by continuous specific heat capacity c_p, thermal conductivity k and density ρ. Considering a continuum is the approach adopted in all previous studies and is justified by the dimension of the probed zone (0.7 mm laser diameter in our case), which is much larger than possible nanoscale heterogeneities, even for nanoporous media as the synthetic soot samples studied here. Space- and time-resolved temperature profiles were calculated with the 3D heat conduction equation:

$$\rho(T)\cdot c_p(T)\frac{\partial T(x,y,z,t)}{\partial t} = k(T)\left(\frac{\partial^2 T(x,y,z,t)}{\partial x^2} + \right.$$
$$\left. + \frac{\partial^2 T(x,y,z,t)}{\partial y^2} + \frac{\partial^2 T(x,y,z,t)}{\partial z^2}\right) + q_H(x,y,z,t) \tag{8}$$

where T is the local sample temperature as a function of the time t and position (x, y, z). The term $q_H(x,y,z,t)$ describes the heat source which, in this case, is the desorption laser pulse. To match the characteristics of the laser pulse used in the experiments, the heat source is represented as a flat space profile (equivalent to a top-hat laser profile) in the calculations. In the temporal domain, the laser beam is represented as a Gaussian pulse. The energy of the laser pulse is absorbed by the sample according to the Beer-Lambert law, therefore:

$$q_H(x,y,z,t) = \alpha\, I_0\,(1-R)\cdot f(x,y)\cdot g(t)\cdot e^{-\alpha z}$$

$$f(x,y) = \begin{cases} 1, & \sqrt{x^2+y^2} \le r_{des} \\ 0, & \text{otherwise} \end{cases} \tag{9}$$

$$g(t) = \frac{1}{\sigma\sqrt{2\pi}}\cdot \exp\left[-\frac{1}{2}\left(\frac{t-t_0}{\sigma}\right)^2\right], \quad \text{with } \sigma = \frac{\tau_{des}}{2\sqrt{2\ln 2}} \tag{10}$$

where R is the sample surface reflectivity, α is the adsorption coefficient at the desorption wavelength (532 nm), I_0 is the pulse peak irradiance. The $f(x,y)$ and $g(t)$ functions define the space and time profiles of the pulsed laser beam of radius r_{des} (top-hat) and duration τ_{des} (full width at half maximum, Gaussian). Previous studies conducted by multi-wavelength pyrometry [40] showed no change in the structural or optical properties of similar carbonaceous surfaces for a laser-induced transient temperature increase of more than 2000°C, which is above the maximum temperatures reached here. Accordingly, the R and α parameters were kept constant in the calculations. The same approach is sometimes adopted for simulating the laser-induced incandescence (LII) of soot nanoparticles, where even higher temperatures (4000 K) are reached [67]. Moreover, Eqs. (8) and (9) do not include any terms accounting for phase transitions or surface alteration (*e.g.* photo/thermal-bleaching) [68] as these do not occur at the low desorption fluence values studied here. The boundary conditions required to solve Eq. (8) are:

$$\begin{cases} T(x\to\infty, y\to\infty, z\to\infty, t) = T_i \\ T(x,y,x,t=0) = T_i \end{cases} \tag{11}$$

where T_i is the initial temperature of the sample.

The thermal conductivity of nonporous samples (*e.g.* graphite) can be found in the literature [58]. For porous materials, such as nano-porous soot (*nps*), the thermal conductivity k_{nps} strongly depends on the porosity as the efficiency of phonon propagation is related to the number of contact points between the nanoparticles forming the sample. In this case, the thermal conductivity k_{nps} of

the *nps* layer can be expressed as [69]:

$$k_{nps}(T) = k_{graph}(T)\left[(1-\xi)^{3/2} + \xi^{1/4}\frac{k_{air}(T)}{k_{graph}(T)}\right] \quad (12)$$

where k_{graph} is the thermal conductivity of bulk graphite [58] and k_{air} is the conductivity of the air filling the pores. The layer porosity ξ is given by:

$$\xi = 1 - \frac{\rho_{nps}}{\rho_{graph}} \quad (13)$$

where ρ_{nps} and ρ_{graph} are the densities of nano-porous soot and graphite, respectively.

The parameters required to calculate the temperature profile of the studied sample were either taken from the literature [11, 26, 58, 63, 69, 70] or calculated from the values for graphite while accounting for the porosity of the sample (Eqs. (12), (13)). The temperature variations of all parameters required for solving Eq. (8) are presented in Fig. S2 of the Supplementary Material. Physical parameters for the graphite sheet and HOPG samples used in this work are nearly identical which allows us to use the same physical characteristics for these two sets of samples.

Eq. (8) was solved with the COMSOL Multiphysics simulation platform using finite element methods. The temporal and spatial temperature evolutions calculated for nano-porous soot and graphite (Fig. 3) show a fast increase with a maximum value reached at t = 5.5 ns in the center of the irradiated surface, followed by a slower cooling toward the initial sample temperature (on microsecond timescale). The heat-affected sample depth is in the range of 100 μm (Fig. 3b), which is significantly lower than the thickness of the samples used in this study. We note that the obtained depth and temporal profiles follow the same trend as the ones reported by previous similar studies [49, 63, 64], although a direct, quantitative comparison is not possible, as the temperature profiles reported in the literature were computed for different materials and desorption laser characteristics (*e.g.* wavelength, pulse duration, fluence).

3.4.2. Time- and space-resolved desorption

Once the temperature profile $T(x, y, z, t)$ is calculated, a space- and time-resolved desorption mathematical model, including the time-dependence of the desorption rate, the number of molecules desorbed per unit of surface, and the total number of molecules desorbed after each desorption pulse can be formulated.

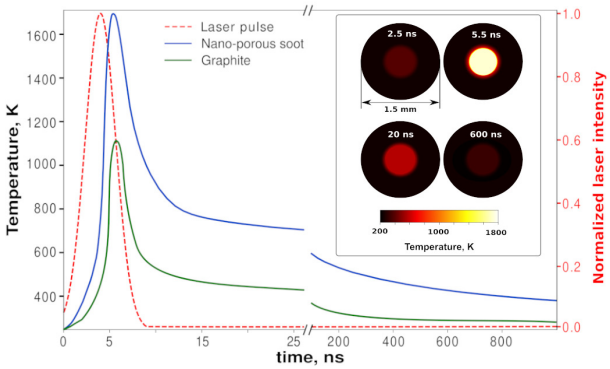

Figure 3: Temporal evolution of the temperature in the center of the irradiated spot $T(x = 0, y = 0, z = 0, t)$ calculated for nano-porous soot (blue lines) and graphite (green lines) obtained for $F_{des} = 32$ mJ cm^{-2}. The temporal profile of the desorption laser is plotted for comparison (red dashed line). Snapshots of the radial distribution of the temperature at various delays after the laser pulse are presented in the inset.

The number of molecules desorbed from the surface after the first laser pulse can be therefore expressed as follows:

$$N_1 = \iint_{-\infty}^{+\infty} Q_0(x,y)\cdot\left(1 - \exp\left(-\nu\int_0^{\frac{1}{f}}\exp\left(-\frac{E_{ads}}{k_B T(x,y,z=0,t)}\right)dt\right)\right)dxdy \quad (14)$$

where Q_0 is the initial adsorbate surface concentration and f is the repetition rate of the desorption laser. The number of molecules desorbed on the j^{th} desorption pulse can thus be determined with the following relationship:

$$N_j = \iint_{-\infty}^{+\infty} Q_{j-1}(x,y)\cdot\left(1 - \exp\left(-\nu\int_0^{\frac{1}{f}}\exp\left(-\frac{E_{ads}}{k_B T(x,y,z=0,t)}\right)dt\right)\right)dxdy \quad (15)$$

$Q_{j-1}(x, y)$ represents the analyte surface concentration after the $(j-1)^{th}$ desorption pulse (*i.e.* before the jth desorption pulse). Since the surface concentration of the analyte decreases after each desorption pulse, the number of desorbing molecules is progressively reduced.

Once a proportionality factor m is introduced to take into account the overall detection efficiency, the equation can be used for experimental data fitting and adsorption energy retrieval:

$$S_j = m \cdot N_j = m \cdot \iint_{-\infty}^{+\infty} Q_{j-1}(x,y) \cdot \left(1 - \exp\left(-\nu \cdot \int_0^{\frac{1}{f}} \exp\left(-\frac{E_{ads}}{k_B T(x,y,z=0,t)}\right) dt\right)\right) dxdy \quad (16)$$

where S_j is the signal recorded by the detector for the j^{th} desorption pulse. The only unknowns in this equation are the pre-exponential factor ν, the adsorption energy E_{ads}, and the proportionality factor m. Similarly to the "effective temperature" model, the adsorption energy is determined by fitting the experimental data, in this case with Eq. (16). Compared to the "effective temperature" model, the correlation between the unknown parameters in this equation is much lower which facilitates the fitting procedure. Initial adsorption energy values were sourced from the literature and were the same as in the effective temperature model fits (see above). The initial value for the pre-exponential parameter was taken in accordance with literature recommendations [42, 53, 71] as $\nu = 10^{12}\,\mathrm{s}^{-1}$.

3.5. Data fitting

Fitting the experimental data can be challenging as some of the unknown parameters (*e.g.* E_{ads} and B in the "effective temperature" model) are highly correlated. Least-square fitting with functions that contain highly correlated parameters and/or multiple exponential functions can be very unstable, as the outcome of the fit is highly dependent on the initial guess. A *search method* [72] could be used in this case – an algorithm relying on multiple least-square fits of the data performed with different initial values (in user-defined ranges) of the unknown parameters. However, this method is characterized by a rather long convergence time and relatively wide posterior distribution of the retrieved values, and thus was not used here. Instead, we adopted a Markov chains Monte Carlo (MCMC) fitting approach (described in Appendix A) in a Bayesian statistics framework. Starting with initial values for fitted parameters sourced from literature (or calculated based on literature data), several hundred thousands fits are generated to match the experimental data using both the steady-state and transient models. This procedure will return posterior distributions for the fitted parameters. The mode of these distributions will represent the most probable fit for the given dataset and the confidence intervals will reflect the precision of determination of the unknown parameters from the fit. An illustration is given in Fig. 4 for the signal decay of pyrene adsorbed on activated carbon nanoparticles (experimental data averaged over four desorption spots on the same sample, 2σ error bars) fitted with the steady-state and the transient temperature models. We notice that both models fit equally well the experimental data, however it is important to emphasize that the red (steady-state model) and green (transient model) dashed lines in Fig. 4a reflect two distinct mathematical concepts. The former results from a severe approximation in that the desorption process occurs at a constant ("effective") surface temperature, whereas the latter more closely represents the physical reality in that the surface temperature evolves in time and space during the desorption process. The 95% credibility intervals highlighted on the E_{ads} posterior distributions displayed in Fig. 4b clearly reflect the much lower correlation of the fitted parameters in the transient model with respect to the steady-state one. However, these intervals cannot be used directly to derive "physically-significant" error bars for the adsorption energy, as the developed MCMC fitting algorithm could not converge in a reasonable number of steps (500 000) when large error bars are specified for the experimental data. To derive physically-significant error bars of the fitted parameters, we fitted multiple individual datasets generated from the same sample in the same experimental conditions (see Section 2.5) and further applied an "aggregation of estimators" procedure (see Appendix B) to the fitted parameters values and variances.

4. Results

4.1. Polycyclic aromatic hydrocarbons on activated carbon nanoparticles

The experimental approaches and the associated mathematical models are first tested using "synthetic soot" samples synthesized in the laboratory (Section 2.4) by (co)adsorbing polycyclic aromatic hydrocarbons on activated carbon nanoparticles at well-controlled, sub-monolayer surface coverages. Pyrene ($\mathrm{C_{16}H_{10}}$) and coronene ($\mathrm{C_{24}H_{12}}$) were chosen as representative PAHs as they are both known

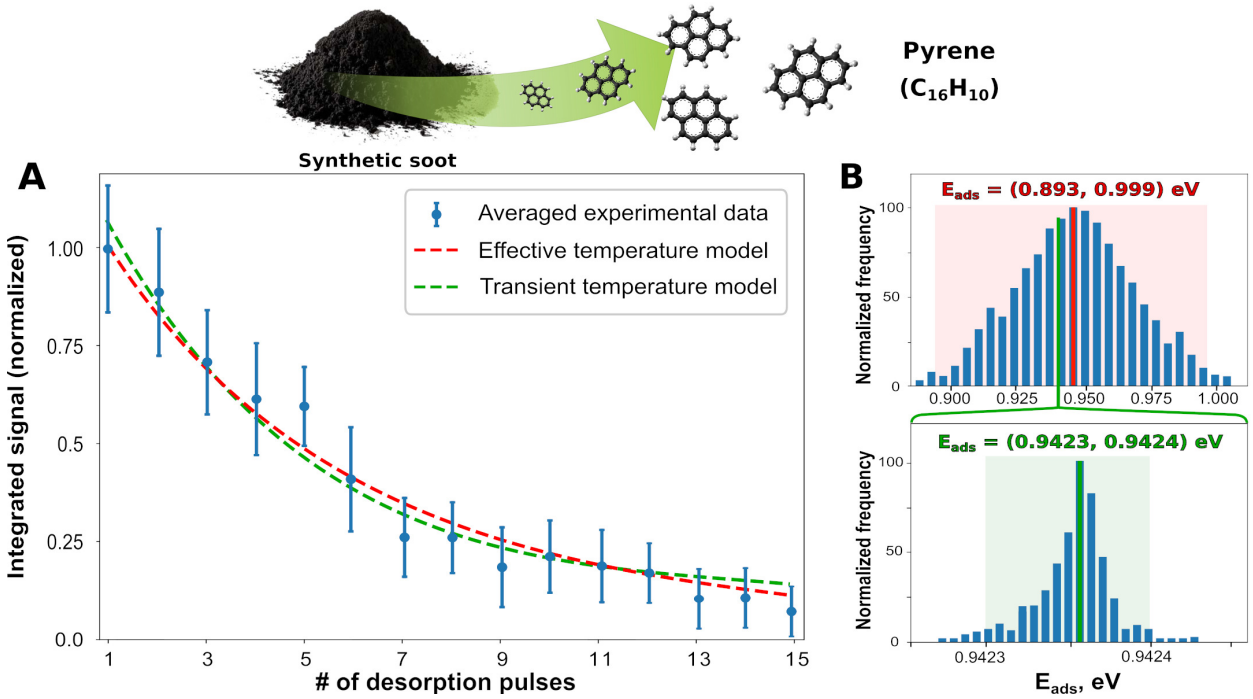

Figure 4: (a) Steady-state (red dashed line) and transient (green dashed line) models fitted to the signal decay curve (four-zone average experimental datapoints) of pyrene desorbing from activated carbon (F_{des} = 32 mJ cm^{-2}). The plotted fits correspond to the maximum (mode) of the Bayesian posterior distributions shown in (b) – top: steady state, bottom: transient. Shaded areas represent the 95% credibility intervals of E_{ads}.

to be present on combustion generated soot particles [11–13, 30] and, at the same time, exhibit significantly different adsorption energies, which makes them perfect candidates to test the E_{ads} recovery method. Two sets of samples were synthesized, the first one with a single adsorbed PAH (pyrene), the second one with both PAHs co-adsorbed on the same surface. The proposed method allows measuring adsorption energies of co-adsorbed species, as the signal of multiple mass peaks can be simultaneously monitored by time-of-flight mass spectrometry.

4.1.1. Pyrene

Multiple signal decay and fluence curve datasets are recorded from the pyrene / activated carbon surface following the approach described in Section 2.5 and the MCMC fitting procedure is applied to these individual datasets for both steady-state and transient models. The E_{ads} initial value was taken as 0.98 eV from the literature [60] and this parameter was allowed to vary in the 0.6–1.2 eV interval for both models. For the steady-state model, an initial B value of 26 J^{-1} K m^2 (Table 2) is used, with an allowed variation interval 15–30 J^{-1} K m^2. In the transient model, a 10^{12} s^{-1} initial value is considered for the pre-exponential parameter ν in accordance with literature recommendations [53, 71], along with the allowed variation interval 10^{11}–10^{13} s^{-1}. Starting with these values, a maximum of 100 000 fits are generated to match the individual datasets with the steady-state and transient models. Both models converge before reaching the maximum number of allowed fits, typically in ∼50 000 steps each. The posterior distributions of the E_{ads}, B, and ν parameters returned by individual fits are aggregated following the procedure described in Appendix B to calculate the average values and associated error bars (1σ) listed in Table 3. The obtained data is then used to reconstruct the signal decay and fluence curves, as illustrated in Fig. S3 of the Supplementary Material.

We notice an excellent agreement between the adsorption energies found in both experimental approaches (both signal decay and fluence curve) and by both models. These results are also well in line with the literature value measured for pyrene ad-

sorbed on soot particles using thermal desorption kinetics (0.986 eV) [60]. For the "effective temperature" model the B parameters returned by the two approaches ($B_{decay} = 23.9 \pm 3.4$ J^{-1} K m^2 and $B_{fluence} = 21.3 \pm 2.1$ J^{-1} K m^2) are in good agreement with each other and slightly smaller than the initial estimation (26 J^{-1} K m^2) calculated using literature values. For the transient temperature model, the retrieved pre-exponential factor ν ($1.56{\cdot}10^{12}$ s^{-1}) is also close to the initial guess. Beside validating the analytical method proposed here, the good agreement with previous works also confirms that the analyzed samples mimic well soot samples described in the literature.

4.1.2. Pyrene and coronene co-adsorbed

Having demonstrated functionality with a single PAH adsorbed onto activated carbon, this adsorption energy calculation method is then put to test using a system consisting of two different polycyclic aromatic compounds co-adsorbed onto the same adsorbant but in such low amount (10^{-3} – 10^{-2} monolayer) that any lateral interactions between them can be neglected. In this configuration, the same laser pulse applied to the surface will lead to the desorption of both molecules, but each with its own kinetics (determined by its adsorption energy value). Signals associated with both molecules are simultaneously recorded by the mass spectrometer to generate individual datasets which are further subjected to the fitting procedure described above, leading to the results displayed in Table 3.

For the adsorption energy of pyrene, we observe again a very good agreement between the values retrieved by the various experimental / theoretical approaches and also with the values determined above, when pyrene was the sole analyte adsorbed onto activated carbon. For coronene, the adsorption energy values determined from various approaches are in excellent agreement with each other and in line with those experimentally determined via temperature programmed desorption measurements for coronene adsorbed on carbon nanofibers (1.31–1.50 eV) [42]. The signal decay and fluence curves of both pyrene and coronene reconstructed from parameters presented in Table 3 overlayed on experimental data are illustrated in Fig. S4 of the Supplementary Material. The B parameters (characteristic of the adsorbent) determined from the two fits of the binary adsorbate / activated carbon sample are in close agreement with each other and also with the ones retrieved for the previous single adsorbate system (pyrene / activated carbon) sharing the same adsorbent. Similarly, the ν parameter for pyrene agrees well between the two systems. Coronene shows a higher ν value (with respect to pyrene), as expected from theoretical calculations [53, 71]. These results demonstrate the robustness of the adsorption energy calculation method from LITD experiments and allow us to conceive its extension to other adsorbate/adsorbent systems.

4.2. Pb on activated carbon nanoparticles

Heavy metal ions (*e.g.* Pb^{2+}) are common contaminants of industrial wastewater and are usually removed using various carbonaceous materials [9, 10]. Thus, the study of the interaction between heavy metals, proven to be carcinogenic even at low concentration, and materials used for their removal from water (*e.g.* activated carbon) is of great importance. Detection of lead on soot particles (presumably coming from combustion of leaded gasoline) was already shown to be possible with laser-based mass spectrometry (*e.g.* Particle Analysis by Laser Mass Spectrometry, PALMS) employing UV ionization of desorbed species [73, 74]. $PbCl_2$ salt was dissolved in deionized water and the resulting solution was used to impregnate the activated carbon nanoparticles. Mass spectra recorded upon sample irradiation with the 532 nm laser and ejecta ionization with the 266 nm laser exhibited the characteristic isotopic distribution of Pb^+ in the m/z 204–208 range, presented in Fig. S5 of the Supplementary Material. No Pb^{2+} signal was present in the mass spectra. Moreover, experiments performed with the ionization laser switched off gave no signal in the mass spectra, *i.e.* ionized lead is not directly sampled from the surface. This may seem surprising, as Pb^{2+} ions may be formed in the aqueous solution and be further transferred onto the adsorbent surface. Our explanation for this is twofold. First, the desorption fluence employed (limited by the carbonaceous surface ablation threshold) might be too low for desorbing these ions from the surface. Second, the formation of Pb^{2+} in the aqueous solution is only one of many other possibilities, as Pb–Cl is not a "pure" ionic bond ($\Delta\chi_{Pb-Cl} < 1.7$). Furthermore, in aqueous solution the formation of an array of (partially) solvated ions is to be expected. All these ions can then adsorb onto activated carbon via different mechanisms (adsorption, surface precipitation, ion exchange, sorption, etc.) [10, 75–79], and participate to further acid/base,

Table 3: Main parameters derived with the "effective" and transient temperature models. Mean values and error bars are computed using the procedure described in Appendix B. The small number of experimental points for the fluence curve of the pyrene/HOPG system prevented a reliable derivation of the adsorption energy from its fluence curve.

Absorbate	Sample	"Effective temp." model				Transient temp. model	
		Signal decay		Fluence curve		Signal decay	
		E_{ads}, eV	B, $J^{-1}\,K\,m^2$	E_{ads}, eV	B, $J^{-1}\,K\,m^2$	E_{ads}, eV	ν, 10^{12} s^{-1}
Pyrene	Pyrene / activated carbon	0.949±0.049	23.9±3.4	0.968 ± 0.041	21.3 ± 2.1	0.965±0.014	1.56±0.21
	(Pyrene + coronene) / activated carbon	0.961±0.054	20.4±2.8	0.983 ± 0.038	22.4 ± 2.5	0.958±0.018	1.31±0.34
	Pyrene / graphite sheet	0.681±0.019	14.1±1.9	0.662 ± 0.015	15.1 ± 1.4	0.696±0.010	1.24±0.18
	Pyrene / HOPG	0.476±0.021	13.5±1.9	–	–	0.508±0.011	1.38±0.13
Coronene	(Pyrene + coronene) / activated carbon	1.519±0.022	22.8±2.4	1.508 ± 0.024	23.1 ± 1.1	1.513±0.013	2.46±0.15
Pb	Pb / activated carbon	0.226±0.024	20.6±2.3	0.206 ± 0.015	21.1 ± 2.1	0.243±0.011	7.46±0.26

redox or coordination reactions on the particle surface. A thorough investigation of such a complex surface chemistry is well beyond the scope of the present work.

Both experimental approaches (signal decay and fluence curve) were applied to study the desorption of lead from activated carbon particles. For the signal decay approach, the recorded signal vanishes in fewer desorption pulses compared to aromatic species adsorbed on the same adsorbent (Fig. S6, Supplementary Material). Fitting both models to the experimental data resulted in values for the adsorption energy (E_{ads}^{steady} = 0.226 eV and $E_{ads}^{transient}$ = 0.243 eV, Table 3) close to that found in the literature (0.21 eV for Pb(II) adsorbed on carbon particles obtained from bio waste) [10]. A similar value ($E_{ads}^{fluence}$= 0.206 eV) was also determined from the fluence curve (Fig. S6, Table 3). The adsorption energy of lead to carbonaceous surfaces is therefore much lower compared to that of aromatic species [10]. The B parameter (which is only related to the adsorbent material) is in good agreement (within the limits of the error bars) with the values returned by the steady-state fits on the other samples involving activated carbon (see Table 3). The pre-exponential factor determined from the transient model fit ($\nu = 7.5{\cdot}10^{12}$ s^{-1}) is in line with theoretical values calculated for small adsorbates [53]. To the best of our knowledge, no ν experimental value for this system is reported in the literature.

4.3. Toward the systematic exploration of adsorption energies as a function of adsorbent properties

In order to expand the adsorption energy calculation method to systems of much greater chemical or structural complexity, it is first necessary to explore various adsorbate/adsorbent systems exhibiting significantly different adsorption energies. This can be realized by testing either distinct adsorbates on the same adsorbent or, conversely, the same adsorbate on distinct adsorbents, the latter being studied here. The adsorption energy retrieved corresponds to the average energy of all desorbed molecules. If the irradiated surface contains different types of adsorption sites, each one characterized by a different adsorption energy, then the measured E_{ads} can be expressed as a weighted average of all possible energy values (*i.e.* energies that correspond to all existing sites). The change in the proportion of adsorption sites of a given type will modify the average and hence the measured (desorption spot averaged) adsorption energy.

Various surface defects can act as adsorption sites (*e.g.* vacancies, impurities) and most of them are present and abundant on the surface of synthetic (and real) soot particles. The adsorption energy of aromatic compounds on adsorbents exhibiting defect-rich surfaces is higher than that expected when the same compounds are adsorbed on a defect-free carbon lattice [80–83]. Accordingly, as the surfaces of materials such as graphite and HOPG contain a much smaller density of defects compared to activated carbon, the adsorption energy of *e.g.* pyrene, on such adsorbents is expected to be substantially lower.

As predicted, the shape of the signal decay curve and the adsorption energy of pyrene desorbed from a graphite sheet and HOPG are noticeably different (Fig. 5). Since the adsorption energy is lower, a smaller number of laser pulses are required to desorb all molecules present on the irradiated spot, hence a shorter signal decay curve is observed. The adsorption energies obtained from the fits performed with the two models (steady-state and transient) are, once again, very similar. Adsorption en-

ergies obtained for pyrene adsorbed on HOPG (Table 3) are in line with values resulting from ab initio calculations (0.42 – 0.5 eV) [80, 81]. To the best of our knowledge, no experimental measurement for either system (pyrene/HOPG or pyrene/graphite sheet) is reported in the literature. When the adsorbent is graphite sheet, the adsorption energy value obtained for pyrene ranges between the ones retrieved for activated carbon and HOPG, which is expected since the surface contains an intermediate number of defects compared to HOPG (fewer defects) and activated carbon (more defects). It is also possible to obtain "fluence curves" for pyrene desorbing from graphite and retrieve the adsorption energy and B parameter from this approach (Table 3). The values for E_{ads} and B (0.681 eV and 14.1 $J^{-1}\,K\,m^2$, respectively) are also in line with the values obtained from the signal decay. Moreover, the obtained B values are close to that calculated with literature parameters (16.2 $J^{-1}\,K\,m^2$, Table 2).

Across the various adsorbate-adsorbent systems investigated here (Table 3), the values obtained and trends followed for B and the pre-exponential ν parameters are in accordance with what should be expected in regards of their relationship with either the adsorbate or the adsorbent. Specifically, as the B parameter is associated with adsorbent properties (for low adsorbate coverages as studied here), its retrieved value should be comparable for all systems featuring the same adsorbent. This is indeed what is observed in Table 3, since a similar B value was obtained with two different experimental approaches for all cases where desorption from the same adsorbent is studied (*e.g.* 20.4 – 23.9 $J^{-1}Km^2$ for activated carbon, Table 3). In contrast, as the pre-exponential factor ν is related to the vibration of the adsorbate-adsorbent bond along the reaction coordinate associated with desorption [53], its value should be largely affected by the adsorbate properties. In accordance, Table 3 shows that the value of this parameter significantly varies for systems based on the same adsorbent but different adsorbates (*e.g.* $1.56{\cdot}10^{12}$ s^{-1} for pyrene adsorbed on activated carbon and $7.46{\cdot}10^{12}$ s^{-1} for lead adsorbed on activated carbon). Such variation with distinct adsorbates was previously reported [42, 53]. Table 3 also confirms that the pre-exponential factor ν values obtained for desorption events involving the same adsorbate are similar (1.24 – $1.56{\cdot}10^{12}$ s^{-1} for pyrene). Finally, beside the consistent evolution of the retrieved ν values across the systems studied here, they are also in good agreement with pre-exponential factors previously reported in the literature.

5. Discussion

While it is possible using microcalorimetry to directly appraise the heat of adsorption of a sorbate on various surfaces with a limit of detection (femtomole) akin to ours, performing measurements on such distinct samples (loose powder to highly oriented surfaces) using a single calorimetric technique can be challenging. A direct comparison with microcalorimetry may be impeded by the fact that we do not study adsorption events taking place from a liquid solution nor directly measure the heat of adsorption of a dose of gaseous molecules onto a powder or a surface, but instead monitor the desorption of 'dry' adsorbates. Temperature-programmed desorption (TPD) measurements can provide reliable estimates for adsorption energies in experimental conditions close to ours (PAHs already adsorbed on the surface, high vacuum pressure conditions). This technique is thus better suited for comparison purposes. The adsorption energies retrieved using our method are in good agreement with the values reported in the literature from TPD measurements or ab initio calculations. To the best of our knowledge, no adsorption energy values determined via (micro/nano)calorimetry techniques are reported in the literature for the adsorbate/adsorbent systems investigated in this work.

The unique features of the new laser-based method proposed here offer some distinct advantages with respect to the more conventional techniques cited above. First, this method can be applied to systems exhibiting micrometer or submillimeter heterogeneities. Specifically, it can be utilized to recover the mean adsorption energy of analytes present in distinct areas of a sample as the lateral resolution is defined by the diameter of the laser spot. The smaller the beam diameter, the better the lateral resolution. Second, our method requires no sample preparation prior to analysis (*e.g.* extraction of material) and necessitates only micrograms of materials to operate. It is hence directly applicable to pristine field-collected and natural samples, for which collecting as much as micrograms of material can be challenging (*e.g.* sampling of aircraft engine [34] or on-road vehicle internal combustion engine emissions [12]). This is particularly important when the focus is on size-selected particles [84, 85] as small as 10 nm, for which the

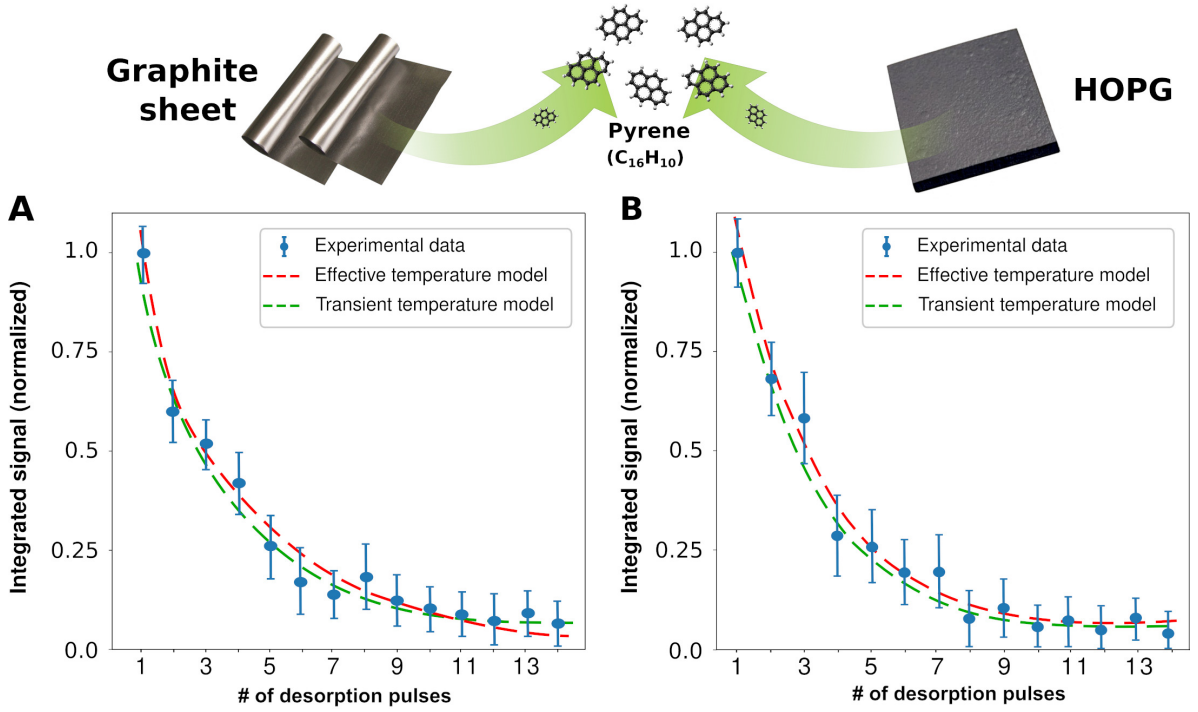

Figure 5: Experimental datapoints (four-zone average) recorded with the "signal decay" approach for pyrene desorbing from (a) graphite sheet (F_{des} = 50 mJ cm^{-2}) and (b) HOPG (F_{des} = 61 mJ cm^{-2}). Steady-state (red dashed line) and transient (green dashed line) decay curves calculated with parameters from Table 3.

particle mass lies within the range of attograms. Third, it allows the simultaneous study of one or several analytes coadsorbed on the same surface, which is particularly adapted to real-world complex mixtures. Finally, these particular characteristics, in conjunction with the very low limit of detection (sub-femtomole) that our method provides, constitute a valuable solution when more conventional techniques cannot be utilized.

The method we present is sensitive enough to show how the structure of the adsorbent (*e.g.* number of defects) can significantly change the mean adsorption energy. As expected, the adsorption energies derived from our experiments increase with the number of surface defects. This method could act as a surface defect probe and monitor defect densities of various adsorbate/adsorbent systems by following a dedicated and systematic experimental procedure. Different adsorption energies averaged over defined zones of a sample surface or between distinct samples can further be related to the disorder/heterogeneity characteristics using, for instance, micro-Raman mapping, where deconvoluted Raman maps can be superimposed on adsorption energy maps of the sample surface probed with the laser. While currently limited to sub-millimeter scale heterogeneities, the lateral resolution could be improved by reducing the diameter of the desorption laser spot size. The high sensitivity of the technique (ensured by the mass spectrometric detection) can be used to finely map spatial variations of physi/chemisorption interactions across heterogeneous samples, possibly containing small surface inclusions (regions with a distinct composition).

The capabilities of the proposed novel method open perspectives of application in various fields. First, it can serve as a benchmark for adsorbate/adsorbent systems against which other methods (*e.g.* ab initio calculations) can be compared. On a technological level, it can also encourage the development of advanced materials specially designed to selectively target and capture dangerous compounds such as toxins or heavy metal ions [86]. Beyond the obvious interest for catalytic or energy storage materials [87], this method can also be used to characterize thin films grown by physical (pulsed laser deposition, magnetron sputtering) [88] or chemical vapor deposition [89] pro-

cesses, which can (depending on the deposition geometry, substrate etc.) exhibit quite large heterogeneities [90, 91] in their adhesion/adsorption properties. The local character of our technique (defined by the laser beam diameter) in conjunction with a fast mathematical treatment (as the simplified effective temperature model) can help in implementing a real-time, spatially-resolved probe directly in the technological process line. Finally, in the combustion field, our method can help shed light on the formation process of soot particles [92, 93] by identifying the origin of the aromatic species present on the surface (i.e. remnants of the nucleation/growth process or condensation from the gas phase).

6. Conclusions

Employing laser-induced thermal desorption in conjunction with an adequate mathematical framework, we successfully determine the adsorption energy of distinct adsorbates deposited onto various carbonaceous surfaces. We first formulate and then apply two different mathematical equations modeling the desorption phenomena observed experimentally. The first model describes the desorption process as a steady state phenomenon, using an "effective" sample temperature. This model, while greatly simplifying the calculations, also only constitutes a rough approximation of the desorption process. Advantageous when computational speed is required, it can be used in conjunction with real-time chemical mapping to better characterize the zone of interest. The second model accounts for the fast variation of surface temperature triggered by the absorption of the laser pulse energy. This transient temperature model is more complex but mathematically describes a scenario much closer to physical reality, and also benefits from very little correlation between the variables. Both models fit our experimental data well and provide results close to the values reported in the literature. The adsorption energy is determined for two organic molecules (pyrene and coronene) as well as for an inorganic adsorbate (lead). This approach is also able to retrieve the energy of different compounds co-adsorbed on the same sample (from the same measurements). This serves as a good "proof of concept" for the method, demonstrating that laser-induced desorption combined with our mathematical formulations can be used to study adsorption mechanisms. The novelty and the advantages of the proposed technique over more traditional approaches in some specific cases along with several new perspectives opened by the developed method were discussed.

Supplementary figures Fig. S1 – S6 can be found in the Supplementary Material at [URL will be inserted by publisher].

Acknowledgments

This work was supported by the French National Research Agency (ANR) under contract ANR-18-CE22-0019 (UNREAL) and through the PIA (Programme d'Investissement d'Avenir) under contracts ANR-10-LABX-005 (LABEX CaPPA - Chemical and Physical Properties of the Atmosphere) and ANR-11-LABX-0007-01 (Labex CEMPI - Centre Européen pour les Mathématiques, la Physique et leurs Interactions). The authors acknowledge Prof. B Capoen for providing access to the UV-Vis spectrofotometer at Centre d' Etudes et de Recherches Lasers et Applications (CERLA) platform at the University of Lille.

Author contribution: DD, CF, AF, MZ conceptualized the experimental and theoretical method. DD, MV, YC executed the experiments, DD, CPirim, YC, CF discussed the results, DD, CPirim, CF wrote the initial version of the manuscript, DD, CPirim, CF, CPreda developed and validated the mathematical model and the statistical approach. All authors revised and approved the manuscript.

Appendix A. Markov chains Monte Carlo data fitting

Fitting experimental data with models involving highly correlated parameters requires the use of Bayesian statistics [94–96], which provide powerful tools for estimating complex models where the maximum likelihood-based estimation methods fail. In this framework, several approaches can be followed. Initial tries with the "conventional" *search method* [72] resulted in rather long convergence times and wide posterior distributions of the retrieved parameters (*e.g.* E_{ads}, B). In this context, we adopted a Markov chains Monte Carlo (MCMC) approach which converges at a much faster pace.

The MCMC method is designed to estimate the joint posterior distribution of a parameter of interest by random sampling in the probability

space. Many problems described by models containing a large number of free parameters, making them expensive to compute with regular methods (*e.g.* problems in cosmology and astrophysics that deal with low signal-to-noise measurements [94–96]), have benefited from MCMC. One of the most important benefits of Bayesian data analysis is the ability to minimize the impact of nuisance parameters [96] – parameters that are required to model the studied process but otherwise are not the main objective of the fit. Most uses of the MCMC are based on the Metropolis-Hastings (M-H) method [94–96] or its derivatives and consist of three main parts:

- Monte Carlo simulations generating random steps to model complex systems.
- Markov chains - sequences of events that are probabilistically related to one another. Each event originates from a set of outcomes and each outcome determines the next one, in accordance with a fixed set of probabilities.
- The acceptance-rejection sampling – an iterative algorithm that generates parameter values from their unknown theoretical posterior distribution.

MCMC allows to generate a data subset covering many possible outcomes of a given system in order to obtain an estimate of the theoretical posterior distribution that can be used to extract statistical measures as mean, median or standard deviation. The simulation process is based on a Markov behavior of the iterative algorithm [95, 96]. An example of a model that can benefit from the use of the MCMC algorithm is the laser-induced thermal desorption, *e.g.* Eq. 6 of the "effective temperature" model that contains a product of two exponential functions and two highly correlated parameters (E_{ads} and B). The performance of the M-H sampler can be very sensitive to the initial choice of parameters. The result of the MCMC fit will be more reliable for longer chains. For this reason, the first values of the Markov chain are usually dropped. Thus, to determine optimal parameters in a data-driven way, a lengthy "burn-in" period must be used. The burn-in allows to start the MCMC procedure with parameters chosen for convenience that might be located in low probability regions, Fig. A.1a. Once the chain has entered the high-probability region, its states become more representative of the correct distribution (the convergence is achieved). All the values after the convergence are then used to retrieve the distributions and mode values of all parameters, Fig. A.1b.

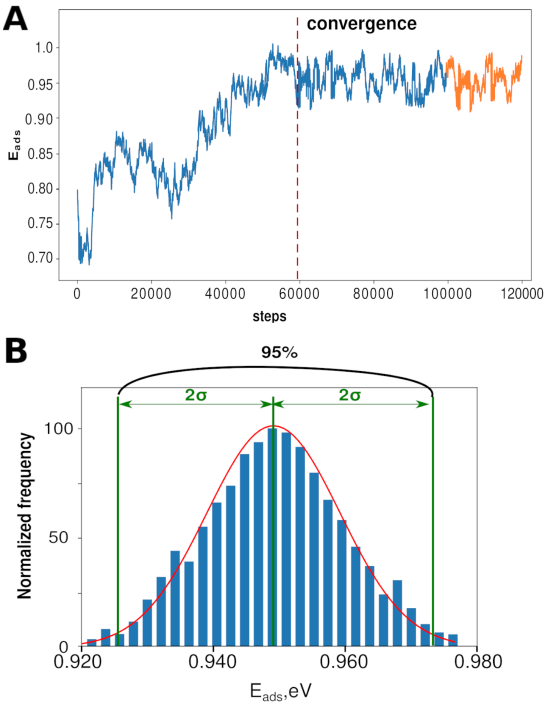

Figure A.1: (a) Example of a Markov chain obtained during fitting of experimental data. The convergence of the fit is depicted with a red dashed line. The last portion of the chain (orange line) is used to determine the posterior distribution of the fitted parameter (b). The distribution is then used to identify the most probable value and the variance of the determined parameter.

Appendix B. Average value and error bar calculation by estimator aggregation

Individual fits performed on multiple independent datasets generated as described in Section 2.5 return estimated values and associated variances for all parameters of interest through the posterior distributions. As an example, Fig. B.1 illustrates the individual fits of four signal decays recorded in the same experimental conditions (the solid lines represent the "most probable fit" (mode) of the Bayesian posterior distribution for each dataset). In order to account for the measurement variability and determine "physically-significant" average values and error bars associated with the fitted parameters (called "estimators" henceforth), the "inter-

nal" (*i.e.* inside one individual dataset) and "external" (*i.e.* between different datasets, such as A, B, C, D zones in the signal decay approach, Fig. B.1) variances must be combined in an "estimator aggregation" methodology [97, 98].

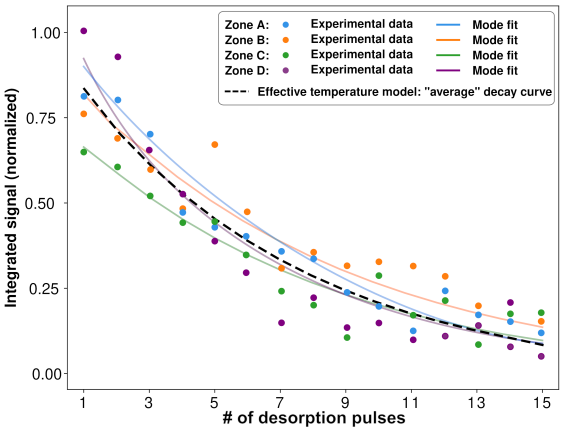

Figure B.1: Symbols: pyrene molecule signal recorded in the same experimental conditions ($F_{des} = 32\ mJ\,cm^{-2}$) from four different zones (A, B, C, D) of the same pyrene / activated carbon sample (homogeneous coverage). Solid lines: most probable (mode) fits returned by the Bayesian posterior distribution for each individual dataset. Dashed line: effective temperature model decay curve generated with average parameter values (Table 3).

For a given parameter $\hat{\beta}$, let $\hat{\beta}_i$ be the estimators obtained from data collected in the zone i, $i \in A, B, C, D$. Then, the best linear-combination estimator for the $\hat{\beta}$ parameter with respect to the mean squared error will be:

$$\hat{\beta} = \sum_{i=1}^{n} \omega_i \hat{\beta}_i \qquad \text{(B.1)}$$

where $\omega_i = \frac{Var^{-1}(\hat{\beta}_i)}{\sum_j Var^{-1}(\hat{\beta}_j)}$ is the weight associated with each estimator, retrieved from fitting individual datasets (either signal decays or fluence curves). Considering the independence of data recorded in different zones of the sample, the standard deviation of the $\hat{\beta}$ parameter is given by:

$$\sigma(\hat{\beta}) = \sqrt{Var(\hat{\beta})} = \sqrt{\sum_i \omega_i^2 (Var(\hat{\beta}_i) + (\hat{\beta}_i - \hat{\beta})^2)} \qquad \text{(B.2)}$$

The first term in Eq. (B.2) represents the "internal" variance of each dataset, while the second term represents the "external" variance (*i.e.* between datasets).

The average values and error bars were calculated for the parameters of interest with the described method and reported in Table 3 in the form $\hat{\beta} \pm \sigma(\hat{\beta})$. The validity of the method can be verified with the "average" fitting curve (*i.e.* average for all datasets) calculated with the average values for the required parameters. An example of such a curve obtained with the "effective temperature" model is presented in Fig, B.1 (dashed line).

References

[1] T. D. Burchell, Carbon Materials for Advanced Technologies, Elsevier Science, Oxford, 1999. doi:10.1016/B978-008042683-9/50002-9.

[2] A. Jorio, G. Dresselhaus, M. S. Dresselhaus, Carbon Nanotubes. Advanced Topics in the Synthesis, Structure, Properties and Applications, Springer Verlag, Berlin, Heidelberg, 2007. doi:10.1071/978-3-540-72865-8.

[3] Z. Zhang, S. Yang, H. Li, Y. Zan, X. Li, Y. Zhu, M. Dou, F. Wang, Sustainable Carbonaceous Materials Derived from Biomass as Metal-Free Electrocatalysts, Adv. Mater. 31 (2019) 1805718. doi:10.1002/adma.201805718.

[4] M. Inagaki, F. Kang, M. Toyoda, H. Konno, Carbon Materials for Adsorption of Molecules and Ions, Adv. Mate. 5 (2014) 335–361. doi:10.1016/b978-0-12-407789-8.00015-6.

[5] M. R. Elamin, B. Y. Abdulkhair, A. O. Elzupir, Insight to aspirin sorption behavior on carbon nanotubes from aqueous solution: Thermodynamics, kinetics, influence of functionalization and solution parameters, Sci. Rep. 9 (2019) 12795. doi:10.1038/s41598-019-49331-6.

[6] M. Ahmaruzzaman, D. Mohanta, A. Nath, Environmentally benign fabrication of SnO_2-CNT nanohybrids and their multifunctional efficiency as an adsorbent, catalyst and antimicrobial agent for water decontamination, Sci. Rep. 9 (2019) 12795. doi:10.1038/s41598-019-49181-2.

[7] S. T. Lim, J. H. Kim, C. Y. Lee, S. Koo, D. Jerng, S. Wongwises, H. S. Ahn, Mesoporous graphene adsorbents for the removal of toluene and xylene at various concentrations and its reusability, Sci. Rep. 9 (2019) 10922. doi:10.1038/s41598-019-47100-z.

[8] M. Darvish Ganji, H. Kiyani, Molecular simulation of efficient removal of H2S pollutant by cyclodextrine functionalized CNTs, Sci. Rep. 9 (2019) 10605. doi:10.1038/s41598-019-46816-2.

[9] A. A. Abia, E. D. Asuquo, Lead (II) and nickel (II) adsorption kinetics from aqueous metal solutions using chemically modified and unmodified agricultural adsorbents, Afr. J. Biotechnol. 5 (2006) 1475–1482.

[10] R. Ahmad, S. Haseeb, Adsorption of Pb(II) on Mentha piperita carbon (MTC) in single and quaternary systems, Arab. J. Chem. 10 (2017) S412–S421. doi:10.1016/j.arabjc.2012.09.013.

[11] A. Faccinetto, C. Focsa, P. Desgroux, M. Ziskind, Progress toward the Quantitative Analysis of PAHs Adsorbed on Soot by Laser Desorption/Laser Ionization/Time-of-Flight Mass Spectrometry,

Environ. Sci. Technol. 49 (2015) 10510–10520. doi:10.1021/acs.est.5b02703.

[12] O. B. Popovicheva, C. Irimiea, Y. Carpentier, I. K. Ortega, E. D. Kireeva, N. K. Shonija, J. Schwarz, M. Vojtíšek-Lom, C. Focsa, Chemical composition of diesel/biodiesel particulate exhaust by FTIR spectroscopy and mass spectrometry: Impact of fuel and driving cycle, Aerosol Air Qual. Res. 17 (2017) 1717–1734. doi:10.4209/aaqr.2017.04.0127.

[13] P. Parent, C. Laffon, I. Marhaba, D. Ferry, T. Z. Regier, I. K. Ortega, B. Chazallon, Y. Carpentier, C. Focsa, Nanoscale characterization of aircraft soot: A high-resolution transmission electron microscopy, Raman spectroscopy, X-ray photoelectron and near-edge X-ray absorption spectroscopy study, Carbon 101 (2016) 86–100. doi:10.1016/j.carbon.2016.01.040.

[14] D. L. Diggs, K. L. Harris, P. V. Rekhadevi, A. Ramesh, Tumor microsomal metabolism of the food toxicant, benzo(a)pyrene, in Apc^{Min} mouse model of colon cancer, Tumor. Biol. 33 (2012) 1255–1260. doi:10.1007/s13277-012-0375-6.

[15] K. H. Kim, S. A. Jahan, E. Kabir, R. J. C. Brown, A review of airborne polycyclic aromatic hydrocarbons (PAHs) and their human health effects, Environ. Int. 60 (2013) 71–80. doi:10.1016/j.envint.2013.07.019.

[16] G. Grimmer, Environmental carcinogens: Polycyclic aromatic hydrocarbons: Chemistry, occurrence, biochemistry, carcinogenicity, CRC Press, New York, 2018. doi:10.1201/9781351071758.

[17] C. A. Pope, D. W. Dockery, Health effects of fine particulate air pollution: Lines that connect, J. Air Waste Manage. Assoc. 56 (2006) 709–742. doi:10.1080/10473289.2006.10464485.

[18] B. A. Maher, I. A. Ahmed, V. Karloukovski, D. A. MacLaren, P. G. Foulds, D. Allsop, D. M. Mann, R. Torres-Jardón, L. Calderon-Garciduenas, Magnetite pollution nanoparticles in the human brain, Proc. Natl. Acad. Sci. U.S.A. 113 (2016) 10797–10801. doi:10.1073/pnas.1605941113.

[19] N. D. Saenen, H. Bové, C. Steuwe, M. B. Roeffaers, E. B. Provost, W. Lefebvre, C. Vanpoucke, M. Ameloot, T. S. Nawrot, Children's urinary environmental carbon load: A novel marker reflecting residential ambient air pollution exposure?, Am. J. Respir. Crit. Care Med. 196 (2017) 873–881. doi:10.1164/rccm.201704-0797OC.

[20] H. Bové, E. Bongaerts, E. Slenders, E. M. Bijnens, N. D. Saenen, W. Gyselaers, P. V. Eyken, M. Plusquin, M. B. J. Roeffaers, M. Ameloot, T. S. Nawrot, Ambient black carbon particles reach the fetal side of human placenta, Nat. Commun. 10 (2019) 3866. doi:10.1038/s41467-019-11654-3.

[21] A. A. Specht, M. W. Blades, Direct determination of polycyclic aromatic hydrocarbons in solid matrices using laser desorption/laser photoionization ion trap mass spectrometry, J. Am. Soc. Mass Spectrom. 14 (2003) 562–570. doi:10.1016/S1044-0305(03)00143-0.

[22] L. Basta, S. Veronesi, Y. Murata, Z. Dubois, N. Mishra, F. Fabbri, C. Coletti, S. Heun, A sensitive calorimetric technique to study energy (heat) exchange at the nanoscale, Nanoscale 10 (2018) 10079–10086. doi:10.1039/C8NR00747K.

[23] C. T. Campbell, J. R. Sellers, Enthalpies and entropies of adsorption on well-defined oxide surfaces: Experimental measurements, Chem. Rev. 113 (2013) 4106–4135. doi:10.1021/cr300329s.

[24] A. Saha, A simultaneous volumetric adsorption–isothermal titration calorimetry study of small molecules on supported metallic nanoparticles, J. Therm. Anal. Calorim. 124 (2016) 1623–1634. doi:10.1007/s10973-016-5262-8.

[25] J. L. Falconer, J. A. Schwarz, Temperature-programmed desorption and reaction: applications to supported catalysts, Cat. Rev. 25 (1983) 141–227. doi:10.1080/01614948308079666.

[26] R. A. Ketola, J. T. Kiuru, V. Tarkiainen, J. T. Kokkonen, J. Räsänen, T. Kotiaho, Detection of volatile organic compounds by temperature-programmed desorption combined with mass spectrometry and fourier transform infrared spectroscopy, Anal. Chim. Acta. 562 (2006) 245–251. doi:10.1016/j.aca.2006.01.069.

[27] J. T. Stuckless, D. E. Starr, D. J. Bald, C. T. Campbell, J. T. Stuckless, D. E. Starr, D. J. Bald, C. T. Campbell, Metal adsorption calorimetry and adhesion energies on clean single-crystal surfaces Metal adsorption calorimetry and adhesion energies on clean single-crystal surfaces, J. Chem. Phys. 107 (1997) 5547–5553. doi:10.1063/1.474230.

[28] W. A. Brown, R. Kose, D. A. King, Femtomole Adsorption Calorimetry on Single-Crystal Surfaces, Chem. Rev. 98 (1998) 797–831. doi:10.1021/cr9700890.

[29] J. H. Fischer-Wolfarth, J. A. Farmer, J. M. Flores-Camacho, A. Genest, I. V. Yudanov, N. Rösch, C. T. Campbell, S. Schauermann, H.-J. Freund, Particle-size dependent heats of adsorption of CO on supported Pd nanoparticles as measured with a single-crystal microcalorimeter, Phys. Rev. B 81 (2010) 241416. doi:10.1103/PhysRevB.81.241416.

[30] A. Faccinetto, P. Desgroux, M. Ziskind, E. Therssen, C. Focsa, High-sensitivity detection of polycyclic aromatic hydrocarbons adsorbed onto soot particles using laser desorption/laser ionization/time-of-flight mass spectrometry: An approach to studying the soot inception process in low-pressure flames, Combust. Flame 158 (2011) 227–239. doi:10.1016/j.combustflame.2010.08.012.

[31] C. Mihesan, M. Ziskind, E. Therssen, P. Desgroux, C. Focsa, IR laser resonant desorption of polycyclic aromatic hydrocarbons, Chem. Phys. Lett. 423 (2006) 407–412. doi:10.1016/j.cplett.2006.04.032.

[32] C. Focsa, J. Destombes, Na/K (H2O) n clusters produced by laser desorption of Na/K salt doped ice, Chemical Physics Letters 347 (2001) 390–396. doi:10.1016/S0009-2614(01)01068-5.

[33] C. Mihesan, N. Lebrun, M. Ziskind, B. Chazallon, C. Focsa, J. Destombes, Ir laser resonant desorption of formaldehyde–H_2O ices: hydrated cluster formation and velocity distribution, Surf. Sci. 566 (2004) 650–658. doi:10.1016/j.susc.2004.06.128.

[34] D. Delhaye, F. X. Ouf, D. Ferry, I. K. Ortega, O. Penanhoat, S. Peillon, F. Salm, X. Vancassel, C. Focsa, C. Irimiea, N. Harivel, B. Perez, E. Quinton, J. Yon, D. Gaffie, The MERMOSE project: Characterization of particulate matter emissions of a commercial aircraft engine, J. Aerosol Sci. 105 (2017) 48–63. doi:10.1016/j.jaerosci.2016.11.018.

[35] L. D. Ngo, D. Duca, J. A. Noble, A. R. Ikhenazene, M. Vojkovic, Y. Carpentier, C. Irimiea, Chemical discrimination of the particulate and gas phases of mini-CAST exhausts using a two-filter collection method, Atmospheric Measurement Techniques 13 (2020) 951–967.

doi:10.5194/amt-13-951-2020.

[36] C. Mihesan, M. Ziskind, E. Therssen, P. Desgroux, C. Focsa, Parametric study of polycyclic aromatic hydrocarbon laser desorption, Journal of Physics: Condensed Matter 20 (2007) 025221. doi:10.1088/0953-8984/20/02/025221.

[37] A. Puretzky, D. Geohegan, G. Hurst, M. Buchanan, B. Luk'yanchuk, Imaging of vapor plumes produced by matrix assisted laser desorption: a plume sharpening effect, Phys. Rev. Lett. 83 (1999) 444. doi:10.1103/PhysRevLett.83.444.

[38] R. Zimmermann, M. Blumenstock, H. J. Heger, K. W. Schramm, A. Kettrup, Emission of nonchlorinated and chlorinated aromatics in the flue gas of incineration plants during and after transient disturbances of combustion conditions: Delayed emission effects, Environ. Sci. Technol. 35 (2001) 1019–1030. doi:10.1021/es000143l.

[39] E. Cappelli, C. Scilletta, S. Orlando, V. Valentini, M. Servidori, Laser annealing of amorphous carbon films, Appl. Surf. Sci. 255 (2009) 5620–5625. doi:10.1016/j.apsusc.2008.10.062.

[40] J. P. Abrahamson, M. Singh, J. P. Mathews, R. L. Vander Wal, Pulsed laser annealing of carbon black, Carbon 124 (2017) 380–390. doi:10.1016/j.carbon.2017.08.080.

[41] S. Ahn, D. Werner, H. K. Karapanagioti, D. R. McGlothlin, R. N. Zare, R. G. Luthy, Phenanthrene and pyrene sorption and intraparticle diffusion in polyoxymethylene, coke, and activated carbon, Environ. Sci. Technol. 39 (2005) 6516–6526. doi:10.1021/es050113o.

[42] R. Zacharia, H. Ulbricht, T. Hertel, Interlayer cohesive energy of graphite from thermal desorption of polyaromatic hydrocarbons, Phys. Rev. B 69 (2004) 155406. doi:10.1103/PhysRevB.69.155406.

[43] R. J. Beuhler, E. Flanigan, L. J. Greene, L. Friedman, Proton transfer mass spectrometry of peptides. rapid heating technique for underivatized peptides containing arginine, J. Am. Chem. Soc. 96 (1974) 3990–3999. doi:10.1021/ja00819a043.

[44] L. P. Levine, J. F. Ready, E. Bernal, Gas desorption produced by a giant pulse laser, J. Appl. Phys. 38 (1967) 331–336. doi:10.1063/1.1708977.

[45] K. Christmann, O. Schober, G. Ertl, M. Neumann, Adsorption of hydrogen on nickel single crystal surfaces, The Journal of Chemical Physics 4528 (1974) 4528–4540. doi:10.1063/1.1680935.

[46] J. M. Chen, C. C. Chang, Laser desorption of submonolayers of Na and Cs from Ge substrates, J. Appl. Phys. 43 (1972) 3884–3886. doi:10.1063/1.1661832.

[47] G. Wedler, H. Ruhmann, Laser induced thermal desorption of carbon monoxide from Fe(110) surfaces, Surf. Sci. 121 (1982) 464–486. doi:10.1016/0039-6028(82)90255-2.

[48] H. Arnolds, C. Rehbein, G. Roberts, R. J. Levis, D. A. King, Femtosecond Near-Infrared Laser Desorption of Multilayer Benzene on Pt(111): A Molecular Newton's Cradle?, J. Phys. Chem. B 104 (2002) 3375–3382. doi:10.1021/jp993688e.

[49] J. L. Brand, S. M. George, Effects of laser pulse characteristics and thermal desorption parameters on laser induced thermal desorption, Surf. Sci. 167 (1986) 341–362. doi:10.1016/0039-6028(86)90709-0.

[50] K. Dreisewerd, M. Schürenberg, M. Karas, F. Hillenkamp, Influence of the laser intensity and spot size on the desorption of molecules and ions in matrix-assisted laser desorption/ionization with a uniform beam profile, Int. J. Mass Spectrom. Ion Process. 141 (1995) 127–148. doi:10.1016/0168-1176(94)04108-J.

[51] K. Oure, V. G. Lifshits, A. A. Saranin, A. V. Zotov, M. Katayama, Surface Science: An Introduction, Springer, Berlin, 2003.

[52] R. M. Bouglas, Principles of adsorption and adsorption processes, Wiley-Interscience publication, New York, 1984.

[53] K. Christmann, Introduction to Surface Physical Chemistry, Springer, Heidelberg, 1991.

[54] L. V. Zhigilei, B. J. Garrison, Molecular dynamics simulation study of the fluence dependence of particle yield and plume composition in laser desorption and ablation of organic solids, Appl. Phys. Lett. 74 (1999) 1341–1343. doi:10.1063/1.123544.

[55] S. Kuper, J. Brannon, K. Brannon, Threshold behavior in polyimide photoablation: Single-shot rate measurements and surface-temperature modeling, Appl. Phys. A 56 (1993) 43–50. doi:10.1007/BF00351902.

[56] W. H. Dalzell, a. F. Sarofim, Optical Constants of Soot and Their Application to Heat-Flux Calculations, J. Heat Transfer 91 (1969) 100. doi:10.1115/1.3580063.

[57] A. B. Djurišić, E. H. Li, Optical properties of graphite, J. Appl. Phys. 85 (1999) 7404–7410. doi:10.1063/1.369370.

[58] R. J. M. Konings, Comprehensive Nuclear Materials, Material Properties - Oxide Fuels for Light Water Reactors and Fast Neutron Reactors, Elsevier, Amsterdam, 2012. doi:10.1016/B978-0-08-056033-5.90001-6.

[59] A. Butland, R. Maddison, The specific heat of graphite: an evaluation of measurements, J. Nucl. Mater. 49 (1973) 45–56. doi:10.1016/0022-3115(73)90060-3.

[60] A. Guilloteau, M. L. Nguyen, Y. Bedjanian, G. Le Bras, Desorption of polycyclic aromatic hydrocarbons from soot surface: Pyrene and fluoranthene, J. Phys. Chem. A 112 (2008) 10552–10559. doi:10.1021/jp803043s.

[61] Y. Bedjanian, M. L. Nguyen, A. Guilloteau, Desorption of polycyclic aromatic hydrocarbons from soot surface: Five- and six-ring (C_{22}, C_{24}) PAHS, J. Phys. Chem. A 114 (2010) 3533–3539. doi:10.1021/jp912110b.

[62] A. Bogaerts, Z. Chen, R. Gijbels, A. Vertes, Laser ablation for analytical sampling: what can we learn from modeling?, Spectrochim. Acta B 58 (2003) 1867–1893. doi:10.1016/j.sab.2003.08.004.

[63] D. Burgess Jr., P. C. Stair, E. Weitz, Calculations of the surface temperature rise and desorption temperature in laser-induced thermal desorption, J. Vac. Sci. Technol. A 4 (1986) 1362 – 1366. doi:10.1116/1.573571.

[64] P. C. Stair, E. Weitz, Pulsed-laser-induced desorption from metal surfaces, J. Opt. Soc. Am. B 4 (1987) 255–260. doi:10.1364/JOSAB.4.000255.

[65] J. Ho, C. Grigoropoulos, J. Humphrey, Computational study of heat transfer and gas dynamics in the pulsed laser evaporation of metals, J. Appl. Phys. 78 (1995) 4696–4709. doi:10.1063/1.359817.

[66] J. Bechtel, Heating of solid targets with laser pulses, J. Appl. Phys. 46 (1975) 1585–1593. doi:10.1063/1.321760.

[67] E. V. Gurentsov, A review on determining the refractive index function, thermal accommodation coefficient and evaporation temperature of light-absorbing nanoparticles suspended in the gas phase using the laser-induced incandescence, Nanotechnol. Rev. 7 (2018) 583–604.

doi:10.1515/ntrev-2018-0080.

[68] J. P. Cummings, J. T. Walsh Jr, Erbium laser ablation: the effect of dynamic optical properties, Appl. Phy. Lett. 62 (1993) 1988–1990. doi:10.1063/1.109512.

[69] W. D. Ciro, E. G. Eddings, A. F. Sarofim, Experimental and numerical investigation of transient soot buildup on a cylindrical container immersed in a jet fuel pool fire, Combust. Sci. Technol. 178 (2006) 2199–2218. doi:10.1080/00102200600626108.

[70] C. Pradère, J.-C. Batsale, J.-M. Goyhénèche, R. Pailler, S. Dilhaire, Thermal properties of carbon fibers at very high temperature, Carbon 47 (2009) 737–743. doi:10.1016/j.carbon.2008.11.015.

[71] K. A. Fichthorn, R. A. Miron, Thermal desorption of large molecules from solid surfaces, Phys. Rev. Lett. 89 (2002) 196103. doi:10.1103/PhysRevLett.89.196103.

[72] X. L. Han, Monte Carlo Least-Squares Fitting of Experimental Signal Waveforms Random Walk Method Testing the Fitting Algorithm, J. Comput. Sci. 4 (2006) 1548–1555, URL: https://digitalcommons.butler.edu/facsch_papers/750.

[73] S. H. Lee, D. M. Murphy, D. S. Thomson, A. M. Middlebrook, Chemical components of single particles measured with particle analysis by laser mass spectrometry (PALMS) during the Atlanta supersite project: Focus on organic/sulfate, lead, soot, and mineral particles, J. Geophys. Res. 107 (2002) AAC1–13. doi:10.1029/2000JD000011.

[74] Y. Zhang, X. Wang, H. Chen, X. Yang, J. Chen, J. O. Allen, Source apportionment of lead-containing aerosol particles in shanghai using single particle mass spectrometry, Chemosphere 74 (2009) 501–507. doi:10.1016/j.chemosphere.2008.10.004.

[75] M. Sekar, V. Sakthi, S. Rengaraj, Kinetics and equilibrium adsorption study of lead (II) onto activated carbon prepared from coconut shell, J. Colloid Interface Sci. 279 (2004) 307–313. doi:10.1016/j.jcis.2004.06.042.

[76] T. A. Saleh, Nanocomposite of carbon nanotubes/silica nanoparticles and their use for adsorption of Pb(II): from surface properties to sorption mechanism, Desalination Water Treat. 57 (2016) 10730–10744. doi:10.1080/19443994.2015.1036784.

[77] E. Bottani, J. M. Tascon, Adsorption of Inorganic Species from Aqueous Solutions. Adsorption by Carbon, Elsevier, Amsterdam, 2008. doi:10.1016/B978-0-08-056033-5.90001-6.

[78] J. P. Chen, X. Wang, Removing copper, zinc, and lead ion by granular activated carbon in pretreated fixed-bed columns, Sep. Purif. Technol. 19 (2000) 157–167. doi:10.1016/S1383-5866(99)00069-6.

[79] K. Kadirvelu, C. Faur-Brasquet, P. L. Cloirec, Removal of Cu(II), Pb(II), and Ni(II) by adsorption onto activated carbon cloths, Langmuir 16 (2000) 8404–8409. doi:10.1021/la0004810.

[80] Y. Zhang, C. Liu, W. Shi, Z. Wang, L. Dai, X. Zhang, Direct measurements of the interaction between pyrene and graphite in aqueous media by single molecule force spectroscopy: Understanding the π-π interactions, Langmuir 23 (2007) 7911–7915. doi:10.1021/la700876d.

[81] C. Ehli, N. Jux, D. Balbinot, G. M. A. Rahman, D. M. Guldi, F. Paolucci, M. Marcaccio, D. Paolucci, M. Melle-Franco, F. Zerbetto, S. Campidelli, M. Prato, Interactions in Single Wall Carbon Nanotubes/Pyrene/Porphyrin Nanohybrids, J. Am. Chem. Soc. 128 (2006) 11222–11231. doi:10.1021/ja0624974.

[82] T. L. Sordo, J. A. Sordo, R. Flórez, Theoretical study of adsorption of hydrocarbons on graphite, J. Comput. Chem. 11 (1990) 291–296. doi:10.1002/jcc.540110303.

[83] J. T. Dickinson, J. J. Shin, S. C. Langford, The role of defects in laser induced positive ion emission from ionic crystals, Appl. Surf. Sci. 96-98 (1996) 316–320. doi:10.1016/0169-4332(95)00436-X.

[84] D. Duca, C. Irimiea, A. Faccinetto, J. A. Noble, M. Vojkovic, Y. Carpentier, I. K. Ortega, C. Pirim, C. Focsa, On the benefits of using multivariate analysis in mass spectrometric studies of combustion-generated aerosols, Faraday Discuss. 218 (2019) 115–137. doi:10.1039/C8FD00238J.

[85] C. Focsa, D. Duca, J. A. Noble, M. Vojkovic, Y. Carpentier, C. Pirim, C. Betrancourt, P. Desgroux, T. Trischer, J. Spielvogel, M. Rahman, A. Boies, K. F. Lee, A. N. Bhave, S. Legendre, O. Lancry, P. Kreutziger, M. Rieker, Multi-technique physico-chemical characterization of particles generated by a gasoline engine: towards measuring tailpipe emissions below 23 nm, Atmos. Environ. 235 (2020) 117642. doi:10.1016/j.atmosenv.2020.117642.

[86] P. A. Turhanen, J. J. Vepsäläinen, S. Peräniemi, Advanced material and approach for metal ions removal from aqueous solutions, Sci. Rep. 5 (2015) 8992. doi:10.1038/srep08992.

[87] S. Cao, B. Li, R. Zhu, H. Pang, Design and synthesis of covalent organic frameworks towards energy and environment fields, Chem. Eng. J. 355 (2019) 602–623. doi:10.1016/j.cej.2018.08.184.

[88] D. Benetti, R. Nouar, R. Nechache, H. Pepin, A. Sarkissian, F. Rosei, J. MacLeod, Combined magnetron sputtering and pulsed laser deposition of TiO_2 and $BFCO$ thin films, Sci. Rep. 7 (2017) 2503–2512. doi:10.1038/s41598-017-02284-0.

[89] H. Matsumura, H. Umemoto, K. K. Gleason, R. Schropp, Catalytic Chemical Vapor Deposition: Technology and Applications of Cat-CVD, Wiley-VCH, Germany, 2019.

[90] J. Perrière, C. Hebert, N. Jedrecy, W. Seiler, O. Zanellato, X. Portier, R. Perez-Casero, E. Millon, M. Nistor, On the relevance of large scale pulsed-laser deposition: Evidence of structural heterogeneities in ZnO thin films, J. Appl. Phys. 116 (2014) 123502. doi:10.1063/1.4896379.

[91] F. Chiarella, C. A. Perroni, F. Chianese, M. Barra, G. M. De Luca, V. Cataudella, A. Cassinese, Post-Deposition Wetting and Instabilities in Organic Thin Films by Supersonic Molecular Beam Deposition, Sci. Rep. 8 (2018) 12015. doi:10.1038/s41598-018-30567-7.

[92] C. Irimiea, A. Faccinetto, X. Mercier, I. K. Ortega, N. Nuns, E. Therssen, P. Desgroux, C. Focsa, Unveiling trends in soot nucleation and growth: When secondary ion mass spectrometry meets statistical analysis, Carbon 144 (2019) 815–830. doi:10.1016/j.carbon.2018.12.015.

[93] C. Irimiea, A. Faccinetto, Y. Carpentier, I. K. Ortega, N. Nuns, E. Therssen, P. Desgroux, C. Focsa, A comprehensive protocol for chemical analysis of flame combustion emissions by secondary ion mass spectrometry, Rapid Commun. Mass Spectrom. 32 (2018) 1015–1025.

doi:10.1002/rcm.8133.

[94] J. Dunkley, M. Bucher, P. G. Ferreira, K. Moodley, C. Skordis, Fast and reliable Markov chain Monte Carlo technique for cosmological parameter estimation, Mon. Not. R. Astron. Soc. 356 (2005) 925–936. doi:10.1111/j.1365-2966.2004.08464.x.

[95] J. Akeret, S. Seehars, A. Amara, A. Refregier, A. Csillaghy, CosmoHammer: Cosmological parameter estimation with the MCMC Hammer, Astron. Comput. 2 (2013) 27–39. doi:10.1016/j.ascom.2013.06.003.

[96] D. Foreman-Mackey, D. W. Hogg, D. Lang, J. Goodman, EMCEE: The MCMC Hammer, Publ. Astron. Soc. Pac. 125 (2012) 306–312. doi:10.1086/670067.

[97] S. T. Buckland, K. P. Burnham, N. H. Augustin, Model selection: an integral part of inference, Biometrics 53 (1997) 603–618. doi:10.2307/2533961.

[98] D. R. Anderson, "Chapter 5: Multimodel inference" in Model based inference in the life sciences: A primer on evidence, Springer Science & Business Media LLC, New York, 2007.